Existence of Charnockites in Hellas Basin, Mars

Authors: Adnan Ahmad[1], Archana M. Nair[1] J. K. Tomson[2] and J. Amal Dev[2]

[1]Earth System Science and Engineering Group, Department of Civil Engineering, Indian Institute of Technology Guwahati, Assam, India

[2]National Centre for Earth Science Studies, Thiruvananthapuram, India

Corresponding author: Archana M. Nair (nair.archana@iitg.ac.in)

Key Points:

- Combined analysis of TIR and VNIR datasets to map charnockitic rocks
- Linear and Polynomial Post Nonlinear mixing models were used for mineral quantification
- THEMIS and CRISM image analysis indicates the existence of charnockites in the Hellas basin

Abstract

Charnockite, an orthopyroxene-bearing granitic rock, is formed under high-temperature and high-pressure environments. Charnockite exhibits spectral characteristics similar to mafic rocks in the VNIR region and shows low emissivity at ~ 8.5 μm due to its high quartz content in the TIR region. The association of charnockite with the Anorthosite-Mangerite-Charnockite-Granite suite make it a suitable planetary analogue. Therefore, this study explores the occurrence of charnockite lithology by identifying coexisting locations of quartz and mafic minerals in the northern region of the Hellas basin of Mars. The study utilises DCS images from Thermal Emission Imaging System (THEMIS) and MAF browse products from the Compact Reconnaissance Imaging Spectrometer for Mars (CRISM) datasets. Spectral characterisation of extracted spectra from both datasets shows the presence of quartz, feldspar, and pyroxene minerals, indicating the possibility of charnockite occurrence on Mars. Spectral mixture analysis using the Linear mixing and the Polynomial-Post nonlinear mixing models confirm the coexistence of quartz, high calcium pyroxene, low calcium pyroxene, and feldspar minerals, providing strong evidence for the presence of charnockitic rocks. The presence of charnockitic rocks indicates possible melting of the mafic crust during the Noachian-aged period. Partial melting of a mafic crust with low water content and high atmospheric carbon dioxide is a possible scenario for the occurrence of charnockite in Hellas Basin. These findings suggest that VNIR and TIR datasets can be combined for mapping charnockite type lithologies on Mars. This study provides valuable insights into the ancient magmatic processes and geologic history of the Martian surface.

1 Introduction

Hellas basin is one of the largest and most ancient impact structures on Mars believed to have formed during the early bombardment in the Noachian period (4.56 to 4.0 Ga; Leonard and Tanaka, 2001; Tanaka et al., 2014). It is a well-preserved impact crater, which spans more than 2300 km across the heavily cratered southern highland on Mars. The region of the Hellas basin comprises ancient highland terrain, extensive channels, and broad volcanic edifices and deposits (Leonard and Tanaka, 2001; Tanaka et al., 2014). Hellas basin has an elevated rim with several rough massifs and mountain ranges and a large partly infilled basin. The basin rim unit is an elevated crust formed during the Early Noachian period, dominated by high crater density (Tanaka and Leonard, 1995). Though most of the regions of the Hellas basin have been dated to the Noachian (4.1–3.7 Ga) and Hesperian periods (3.7–2.9 Ga; Tanaka et al., 2014), the geologic record of the Hellas basin spans all major epochs of Martian chronology. Hellas basin is characterised by the presence of diverse mineralogy such as high-calcium pyroxene (HCP), low-calcium pyroxene (LCP), olivine, clay minerals, sulfates, carbonates, and oxides (Bandfield, 2002; Mustard et al., 2005; Rogers et al., 2009; Skok et al., 2012). Anorthosites and Fe-plagioclase–bearing outcrops are identified in the elevated northern region (Carter and Poulet, 2013; Phillips et al., 2022). The presence of hydrated silica content is identified in the western region of the Hellas basin (Bandfield et al., 2013). The highly diversified mineralogy and spatial distribution of alteration in or around the Hellas basin implies high-grade metamorphism or hydrothermal alteration driven by the impact heating that formed the Hellas basin (Loizeau et al., 2012; Viviano and Phillips, 2019). Moreover, anorthosite and feldspathic rock are orbitally identified across crater peaks of Sytris Major (Bandfield, 2006), crater walls of Hellas basin (Carter and Poulet, 2013; Philips et al., 2022), caldera floor of Nili Patera (Wray, 2013), crater central peaks and intracrater floors of Noachis Terra (Wray, 2013), and feldspar-rich terrains at Terra Sirenum (Payré et al., 2022) on Mars. In addition to anorthosites, Noachian igneous rocks and clasts ranging from trachy-andesite to trachyte and diorite (Sautter et al., 2015; Cousin et al., 2017) are also identified on Mars by in-situ observation from the Curiosity rover. These anorthosite-andesite-diorite associations, along with high-grade metamorphic signatures in the Hellas basin suggest their possible analogy with the Anorthosite-Mangerite-Charnockite-Granite (AMCG) suite that is commonly found in granulite facies terranes on the Earth. However, establishing the presence of AMCG suites in the Hellas basin requires the establishment of the presence of charnockite, which can be achieved by the application of combined analysis of reflectance spectra in VNIR and emissivity spectra in the TIR region.

"Charnockite" sensuo stricto refers to "orthopyroxene-bearing granitoids" (Frost et al., 2001) that are commonly found in regional scale-granulite facies metamorphic terranes. The ongoing debate about the origin of charnockites, i.e, whether they are of magmatic, metamorphic or metasomatic origin (Howie, 1955; Frost and Frost, 2008; Touret and Huizenga, 2012; Samuel et al., 2020) has been addressed in the past few decades by application of multifaceted geochemical-geochronological-isotopic studies (Catlos et al., 2011; Clark et al., 2020). The global type area of charnockite is within the Precambrian Southern Granulite Terrain (SGT) of southern India, which is a regional-scale granulite facies terrain consisting of high-to ultrahigh-temperature metamorphic rocks with ages ranging Archean and Neoproterozoic period (3500-550 Ma)

(Tomson and Dev, 2023 and references therein). In broad consensus, these orthopyroxene-bearing granitoids are expected to be formed in a wide range of tectonic environments; by the melting of a mafic protolith from a subducted slab in the continental arc (Rajesh and Santosh, 2004; Santosh et al., 2017) or by the hydrous partial melting of amphibolitic crust with residual garnet and hornblende in the parental melts (Tomson et al., 2006; 2013) or by the influx of CO_2 rich fluids (Santosh et al., 1991). U-Pb zircon age data of charnockites from SGT identify distinct age populations such as 3.4-3.5 Ga, 2.4-2.6 Ga, 1.9-2.0 Ga, 950-750 Ma and 550 Ma (Santosh et al., 2015;2017; Kumar et al., 2017; Clark et al., 2020; Tomson and Dev, 2023 and references therein). Among these, the 950-750 Ma charnockites associated with anorthosites and granites from the central part of the SGT known as the Madurai block are believed to be formed due to intracrustal melting (Brandt et al., 2014; Dev et al., 2023; Tomson and Dev, 2023). Therefore, these charnockites can be considered as an ideal terrestrial analogue to confirm the presence of the AMCG suite of rocks in the Hellas basin.

The spectral behaviour and diagnostic band position of minerals vary with changes in bulk composition, resulting in wavelength-specific spectral signatures. Subsequently, these spectral signatures have been widely used in identifying, discriminating, and mapping rocks and minerals in the VNIR and TIR regions (Clark, 1999; Nair and Mathew, 2014; Mathew et al., 2009). In the last few decades, technical advancements in airborne and space-borne sensors, as well as subsequent improvements in spatial and spectral resolutions, have helped in modelling the spectral behaviour of terrestrial analogues based on laboratory and in situ spectroscopy (Pompilio et al., 2007; Ehlmann et al., 2011; Nair and Mathew, 2017; Ahmad et al., 2020; Ahmad et al., 2022). Several researchers have carried out qualitative and quantitative studies to remotely observe and interpret outcrops of bedrock on the surface of Earth as analogues and extended the results from the study to remotely identify the surface of Planetary bodies such as the Moon and Mars using spectra of minerals as reference or endmember (Mustard et al., 2005; Ruff et al., 1997; Hamilton and Christiansen, 2000; Hamilton et al., 2001; Pompilio et al., 2007; Poulet et al., 2009; Ehlmann et al., 2012; Nair and Mathew, 2017; Ahmad et al., 2020). Therefore, it is vital to comprehend how the spectral characteristics of the constituent minerals behave in the rock. In reflectance and emittance spectroscopy, the spectral characteristic of rocks is specific to the diagnostic absorption of dominant mineral constituents. Therefore, rocks can be distinguished based on the presence of the major minerals. For example, basalt can be differentiated from granite or granitoid by examining the presence or absence of spectral features that are characteristic of pyroxenes in the VNIR region. Similarly, quartz does not show any diagnostic spectral characteristics in the visible and near-infrared (VNIR) region (Clark, 1999), while it exhibits diagnostic spectral features due to fundamental asymmetric Si–O–Si stretching vibrations in the TIR region.

The mafic rock types, such as basalt and anorthosite, are the most common rock types that have been spectrally identified on the surface of Mars (Adams, 1974; Christensen et al., 2000; Mustard et al., 2005; Wyatt et al., 2001; Poulet et al., 2009; Carter and Poulet, 2013; Rogers and Nekvasil, 2015; Deka et al., 2019; 2020; Phillips et al., 2022). Rarely there are reports of the presence of granites and granitoids. The occurrence of charnockitic rocks on planetary bodies has not been reported so far. In the present study, the spectral characteristics of charnockite were used to identify its possible occurrence on the Noachian-aged Hellas basin on Mars. The presence of anorthosite and silica content in the Noachian-aged northern and western regions of the Hellas basin has been identified in previous studies (Bandfield et al., 2013; Carter and Poulet, 2013; Phillips et al., 2022). Therefore, the Early Noachian highlands and massif highland units in the western Hellas basin and the Middle and Late Noachian highlands of the northern crater rim were selected to evaluate the existence of charnockitic rocks (Figure 1).

For the present study, six regions were selected from the Noachian-aged northern region of the Hellas basin marked as black rectangular boxes (unit 1 to unit 6) (Figure 1b). THEMIS and CRISM datasets of these six regions were further processed for orbital spectroscopy-based mineral composition analysis.

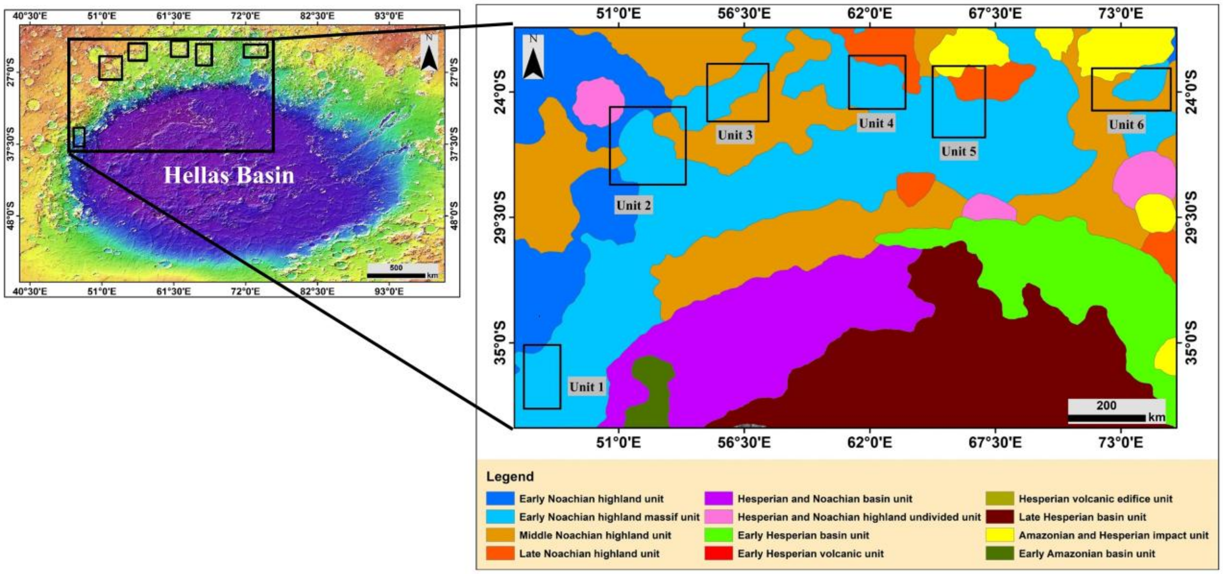

Figure 1 MOLA colour shaded relief map of Hellas basin and Geologic map of the northern region of Hellas basin with areas of interest dated to Noachian age (black rectangular boxes (unit-1 to unit-6)) (modified from Tanaka et al., (2014)).

2 Materials and Methods

2.1 THEMIS Dataset and its Processing

Satellite images of the northern part of the Hellas basin from THEMIS (Thermal Emission Imagining System) onboard Mars Odessey in the TIR region were used to study the surface mineralogy (details of the THEMIS images used in this study are given in Table S1). The THEMIS instrument acquired multispectral datasets consisting of a 5-band with a spatial resolution of 18 m/pixel in the VNIR and a 10-band with 100 m/pixel in the TIR regions (Christensen et al., 2004). The first two bands in the TIR region are similar, with the band centred at 8 μm. These two bands are utilised to improve the signal-to-noise ratio (SNR), while the subsequent bands are centred at 7.9, 8.6, 9.4, 10.2, 11.0, 11.8, 12.6, and 14.9 μm (Christensen et al., 2004). The THEMIS images were selected such that the average surface temperature is ≥ 240 ˚with high SNR values (Bandfield et al., 2004). The surface emissivity data was retrieved using the online THEMIS Processing (THMPROC) utility, which incorporates pre-processing steps as given in Bandfield et al. (2004). Further, to derive the surface emissivity, THEMIS emissivity datasets were corrected for atmospheric CO_2 using TES (Thermal Emission Spectrometer) emissivity data onboard MGS datasets (Christensen et al., 2001). TES atmospheric-corrected emissivity were obtained from ASU

TES data tools (http://tes.asu.edu/data_tool/), following the atmospheric correction method outlined by Bandfield. (2002). The atmospheric component was determined by calculating the ratio between a spectrally uniform region in the THEMIS image and an overlapping TES atmospheric-corrected emissivity spectrum resampled to the THEMIS bandpass. Additionally, assuming that the atmospheric component is constant, it was divided from the entire image or area(s) of interest (Bandfield et al., 2004; Rogers et al., 2007). The THEMIS DCS (Decorrelation stretched) images were obtained using THMPROC with THEMIS bands 8-7-5, 9-6-4, and 6-4-2 in the RGB colour composite (Gillespie et al., 1986). The DCS images highlight spectral variability and unique spectral units can be identified from variations in colour intensity (Gillespie et al., 1986). The spectra were extracted from potential regions identified in the DCS images for spectral matching and quantitative analysis (details of the potential locations of emissivity spectra from THEMIS images used in this study are given in Table S2).

2.2 CRISM Dataset and its Processing

Compact Reconnaissance Imaging Spectrometer for Mars (CRISM) datasets onboard MRO (Mars Reconnaissance Orbiter) in the VNIR region were used to identify the mafic mineralogy in the VNIR region (details of the CRISM images used in this study are given in Table S3). CRISM acquires data in the VNIR wavelength regions of 0.36-3.9 μm with a spectral resolution of 55 nm and a spatial resolution of 15-19 m (Murchie et al., 2007). This study utilises the MTRDR (Map projected Targeted Reduced Data Record) datasets of CRISM to study surface mineralogy. The CRISM MTRDR products are pre-processed datasets that include photometric correction and atmospheric effects (McGuire et al., 2009). The summary products are spectral indices used for surface mineralogy analysis, generated using CRISM Analysis Tools developed by the CRISM Science Team, a plugin to the ENVI software (Exelis Visual Information Solutions, Boulder, Colorado). The negative values of summary products were removed to reduce background noise and emphasise the corresponding minerals. To visualise the spatial variation of surface mineralogy, a thematic RGB composite of the summary product (browse products) is utilised (Viviano-Beck et al., 2014). The spatial distributions of olivine, low calcium pyroxene (LCP) and high calcium pyroxene (HCP) in the study region were obtained using the MAF browse products. The thematic RGB composite of MAF browse product includes OLINDEX3, which indicates an abundance of olivine, LCPINDEX2, which indicates an abundance of LCP and HCPINDEX2, which indicates an abundance of HCP minerals on the surface (Viviano-Beck et al., 2014). The main drawback of the summary product is that it cannot be utilised to determine the quantitative abundance of minerals or to identify minerals. Therefore, in order to identify minerals positively, spectral deconvolution of extracted spectra was carried out. The spectra in the wavelength region of 400 to 2500 nm were extracted from the image at areas that indicated a positive indication of mafic minerals. Further, the target spectrum (average spectrum of several neighbouring pixels) was ratioed to the spectrally flat spectrum extracted from the same detector column to reduce the systematic column-dependent noise and enhance the absorption features (Murchie et al., 2009; Ahmad et al., 2022). The detailed locations of the extract target and flat spectra with kernel size are given in the supplementary Table S4.

2.3 Sample Collection and Spectral Data Acquisition in VNIR and TIR regions

Charnockite samples were collected from three different field outcrops located in Madurai block within Southern Granulite Terrain, India, specifically KK1A from Kodaikanal (10.37°N, 77.54°E), OD1BA from Oddanchataram (10.51°N, 77.82°E) and OD1E from Oddanchatram near Palani Hills(10.47°N, 77.68°E). These samples were thoroughly cleaned in the laboratory to remove any potential contaminants or extraneous matter. Consequently, the cleansed samples were cut into appropriate bulk samples of hand specimens sized for spectral analysis in the VNIR spectral range. The rock samples were crushed using ring mills to obtain powdered samples for spectral analysis in the TIR region.

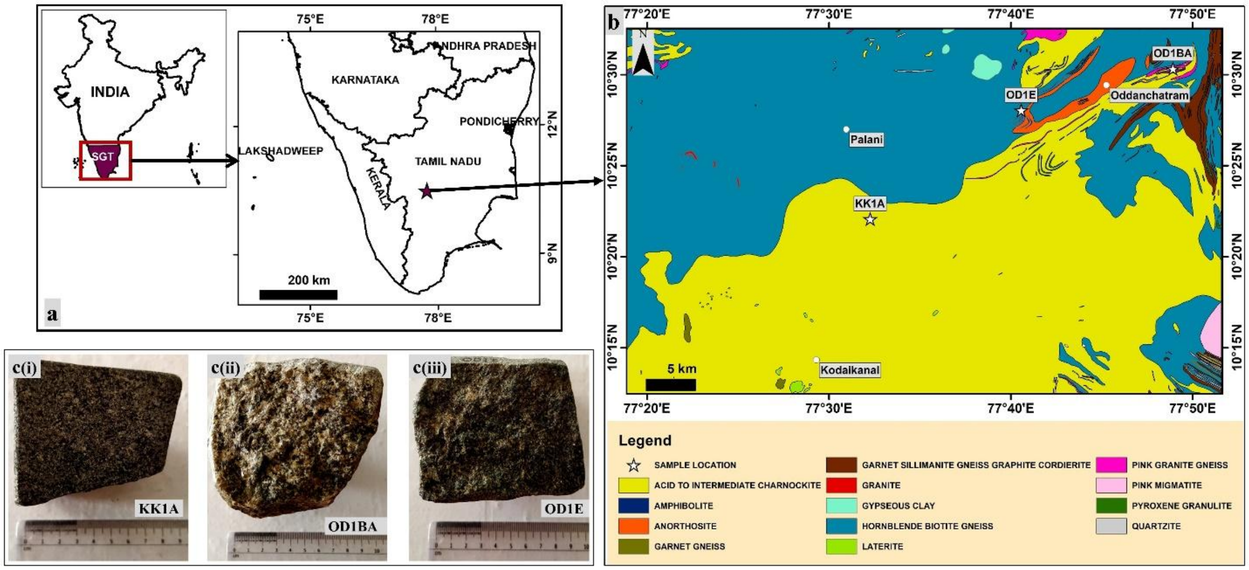

Figure 2 (a) Location of the charnockite samples collection (b) Lithological map of Oddanchatram and Kodaikanal regions within Southern Granulite Terrain, marked with sample collection locations (map modified from Geological Survey of India and accessed from https://bhukosh.gsi.gov.in/). (c) Photographs of charnockite samples, (i) KK1A, (ii) OD1BA, and (iii) OD1E.

The spectra of charnockite samples in the TIR region (7.93-13µm) were acquired using the Fourier Transform Infrared (FTIR) spectroscopy with a Diffuse Reflectance Accessory (DRA). Previous studies have reported that there are no substantial shifts in the position of diagnostic absorption band centres for grain sizes larger than 65 microns, though spectral contrast decreases uniformly (Salisbury and Eastes, 1985; Hamilton and Christensen, 2000). Therefore, the powdered samples with a grain size ranging from 45 to 75 microns were used for spectral measurement in the TIR region. Since FTIR-DRA measured spectra in reflectance mode. Hence, we have used well-established Kirchhoff's Law, i.e., e=1-r (where e is emissivity and r is reflectance) to derive emissivity from reflectance (Salisbury, 1988; Mathew et al., 2009). Further, the spectra of charnockite samples in the VNIR region (350-2500 nm) were acquired using the SVC-HR 768i portable spectroradiometer in a laboratory setup. Here, a 500-W tungsten halogen lamp served as the illumination source in a dark room setup, positioned at a precise angle of incidence at 30° to the sample. A 4° field of view (FOV) lens was utilised to scan the sample samples at a 0° emergence angle.

To ensure the repeatability of the spectra, the spectral acquisition process was replicated multiple times under the same laboratory conditions. The extracted spectra from THEMIS and

CRISM were subsequently validated by comparing them to the laboratory spectra, resampled with the respective wavelength ranges of THEMIS and CRISM datasets.

2.4 Spectral Characterisation

Laboratory spectra of charnockite acquired in the VNIR (400-2500 nm) and TIR (8-13 μm) regions were characterised based on absorption features, and spectra were matched with reference data. For spectral matching and characterisation, reference spectra from the United States Geological Survey (USGS) spectral library were utilised for the VNIR region, and the Arizona State University (ASU) spectral library was used for the TIR region (Christensen et al., 2000; Kokaly et al., 2017). Various spectral parameters like band centre position, band depth, bandwidth, and asymmetry were computed for the laboratory reflectance spectra using DISPEC, an IDL plugin for ENVI (Hecker et al., 2019). The unique absorption features observed in the VNIR and TIR regions are closely linked to the inherent physical and chemical properties of the minerals present (Burns, 1993; Clark, 1999). Rocks and minerals spectra exhibit absorption features in the VNIR region mainly due to the charge-transfer effect, crystal field effect and overtone molecular vibrations (Clark, 1999; Gupta, 2005). Most of the mafic minerals give diagnostic absorption in the VNIR region, such as pyroxene and olivine, exhibit nearly 1000 nm (olivine and pyroxene) and 2000 nm (pyroxene) absorptions due to the crystal field transitions of Fe^{2+} (Burn, 1993; Clark, 1999; Nair and Mathew, 2014). Quartz does not exhibit any diagnostic absorption in the VNIR region. However, in the TIR region, quartz exhibits emissivity minima near 8.5 and 9 µm due to the Si-O-Si asymmetric stretch, and low emissivity between 12 and 13 µm is due to the Si-O-Si symmetric stretch fundamental vibration (Clark, 1999). Felsic rocks exhibit emissivity minima at nearly 9 µm. The mafic rocks exhibit emissivity minima at nearly 10.5-11 µm, which occurs due to Si-0-Si asymmetric stretch fundamental, and a weak emissivity minimum occurs near 12 µm due to symmetric absorption. Anorthositic rocks exhibit emissivity minima at ∼10.4 μm, which is close to the expected mafic composition minima (Lyon, 1965; Clark, 1999; Rogers and Nekvasil, 2015).

This study uses the THEMIS bands 3 to 8 (7.93-11.79 µm) for spectral analysis in the TIR region. The spectra of the THEMIS datasets from the potential region of quartz content were matched with mineral spectra from the ASU spectral library. The spectra from the ASU library were resampled to THEMIS wavelength to validate the presence of corresponding minerals in the region (Figure S1a). Subsequently, spectra of the CRISM datasets from the potential region were matched with the MICA spectral library based on the absorption features to validate the presence of mafic minerals in the region (Figure S1b).

2.5 Spectral Mixture Analysis

Spectra from THEMIS and CRISM datasets were deconvolved into endmember minerals. The fractional abundances of each endmember were derived using spectral mixture models. Due to the predominance of volumetric scattering, the spectral mixture behaves nonlinearly in the VNIR region. Therefore, nonlinear mixing models demonstrate improved accuracy in estimating fractional abundances and reduced reconstruction errors compared to LMM in the VNIR region (Keshava and Mustard, 2002; Dobigeon et al., 2013; Ahmad et al., 2022; Ahmad and Nair., 2024a). In contrast, the spectra behave linearly in the TIR region due to the predominance of surface scattering in this region (Ruff et al., 1997; Poulet and Erard, 2004; Mathew et al., 2009; Dobigeon et al., 2013). In this study, the Polynomial Post-nonlinear mixing (PPNM) model, a linear-quadratic model proposed by Altmann et al. (2012), was used to deconvolve the extracted spectra into their constituent minerals and derive the abundance in the VNIR region. Similarly, in the TIR region, LMM was used to deconvolve and derive mineral abundances.

2.5.1 Linear Mixing Model

THEMIS image-derived spectra were deconvolved into the endmember constituents and their fractional abundance using the LMM. In the LMM, the emissivity spectrum (e) is expressed as a linear combination of N endmembers, each with a corresponding fractional abundance (a). This relationship is represented by equation (1):

$$\boldsymbol{e} = \sum_{\boldsymbol{i}=\boldsymbol{1}}^{\boldsymbol{N}} \boldsymbol{a_i m_i} + \boldsymbol{n_i} = \boldsymbol{Ma} + \boldsymbol{n} \quad \dots \dots \dots (1)$$

In equation (1), $\boldsymbol{e}$ represents the emissivity spectrum vector with dimensions **L × 1**, **M** is an **L × N** matrix containing the **L × 1** endmembers (m_i, i =1....M), **a** is an **M × 1** vector representing the fractional abundances **($\boldsymbol{a_i}$,** i= 1……M**)**, and **n** is an **L × 1** vector denoting additive noise.

Fully Constrained Least-Squares (FCLS) method was used to deconvolve spectra into its fractional abundances constituent of endmembers. FCLS applies two constraints to the fractional abundances. The first constraint subjected to nonnegativity (a_i ≥ = 0, i=1…. M), while the second constraint subjected to full additivity, *i.e.*, sum of fractional abundance is equal to 1 ($\sum_{\boldsymbol{i}=\boldsymbol{1}}^{\boldsymbol{M}} \boldsymbol{a_i} = \boldsymbol{1}$).

The FCLS problem was solved using the SLSQP (Sequential Least Squares Programming) optimisation algorithm, available in the scipy. optimise. minimise module of the SciPy library.

2.5.2 Polynomial Post-Nonlinear Model

In the VNIR region, nonlinear mixing models demonstrate improved accuracy in estimating fractional abundances and reduced reconstruction errors compared to LMM in the VNIR region (Keshava and Mustard, 2002; Bioucas-Dias, 2012; Dobigeon et al., 2013; Ahmad and Nair., 2024b). This study used the PPNM model for nonlinear unmixing on CRISM spectra in the VNIR region. The Polynomial Post-Nonlinear Model (PPNM) is a linear-quadratic model proposed by Altmann et al. (2012). This mixing model for mixing consists of two steps. In the initial step, the spectrum is subjected to linear mixing with the LMM. Subsequently, a polynomial transformation is applied to the resultant spectrum, aiming to introduce nonlinearities. Altmann et al. (2012) consider a second-order polynomial, resulting in a linear-quadratic or bilinear model that accommodates self-interactions. In PPNM, the modelled CRISM reflectance spectrum x is obtained as:

$$\boldsymbol{x} = \boldsymbol{y} + \boldsymbol{b}(\boldsymbol{y} \odot \mathbf{y}) + \mathbf{n} \ldots\ldots\ldots \ (2)$$

$$\boldsymbol{y} = \textstyle\sum_{\boldsymbol{i=1}}^{\boldsymbol{N}} \boldsymbol{a_i m_i} \ldots\ldots\ldots \ (3)$$

Therefore, using the eq (2) and eq (3), the PPNM equation can be rewritten as eq (4)

$$\boldsymbol{x} = \sum_{\boldsymbol{i=1}}^{\boldsymbol{M}} \boldsymbol{a_i m_i} + \boldsymbol{b} \sum_{\boldsymbol{i=1}}^{\boldsymbol{M}} \sum_{\boldsymbol{j=1}}^{\boldsymbol{j=1}} \boldsymbol{a_i a_j m_i m_j} + \boldsymbol{n_i} \ldots\ldots\ldots (4)$$

PPNM includes the self-interaction, and bilinear terms are scaled with the same constant with ∀i , j: b_{ij} = b$\boldsymbol{a_i a_j}$ with no restrictions imposed on the values of b.

The efficacy of LMM and PPNM were evaluated based on root mean square error (RMSE) to measure the error associated between the image-derived spectrum and modelled spectrum, given in eq (5),

$$\boldsymbol{RMSE} = \sqrt{\frac{\boldsymbol{1}}{\boldsymbol{N}} \textstyle\sum_{\boldsymbol{n=1}}^{\boldsymbol{N}} \|\boldsymbol{y_{ns}} - \boldsymbol{\hat{y}_{ns}}\|^{\boldsymbol{2}}} \ldots\ldots\ldots (5)$$

where $\boldsymbol{y_{ns}}$ is an image-derived spectrum and $\boldsymbol{\hat{y}_{ns}}$ modelled spectrum, N is the total number of bands in the spectra.

The endmember reference spectra from ASU and MICA spectral libraries (Figure S1) were used for the deconvolution of extracted spectra from CRISM and THEMIS images. The deconvolved spectra from CRISM and THEMIS images give an idea about the abundance of mafic and quartz minerals at the coexisting locations. In addition, LMM and PPNM model applied to lab spectra resampled to THEMIS in TIR region and CRISM in VNIR region respectively that demonstrated that these models are effective in deconvolving the spectra (Text S1).

3 Results and Discussion

3.1 Laboratory Spectroscopy of Charnockites

Charnockites samples were spectrally characterised in the VNIR region (400-2500 nm). The VNIR reflectance spectrum of KK1A exhibits major diagnostic absorption features at 673.4 nm, 1030.4 nm, and 2321.9 nm (Figure 3a and Table S5). KK1A also shows absorption features at nearly 1437.3 nm and 1974.4 nm, possibly due to overtone O-H vibrations. KK1A spectrum matches well with reference spectra of augite, hornblende, microcline and enstatite (Figure 3a). OD1BA display subdued absorption features at 660 nm and 896.7 nm, broad absorption at 1099.3 nm, conspicuous absorption feature at 1963.5 nm, and narrow absorption at 1429.9 nm and 2303.2 nm. OD1BA spectrum closely matched with reference spectra of oligoclase, albite, microcline, hypersthene and enstatite (Figure 3b and Table S5). OD1E spectrum shows prominent broad absorption features at 999.6 nm and 2298.5 nm. OD1E exhibited narrow conspicuous absorption features at 1969 nm. These absorption features of the OD1E spectrum are matched with reference spectra of augite, pigeonite, hypersthene and microcline (Figure 3c and Table S5).

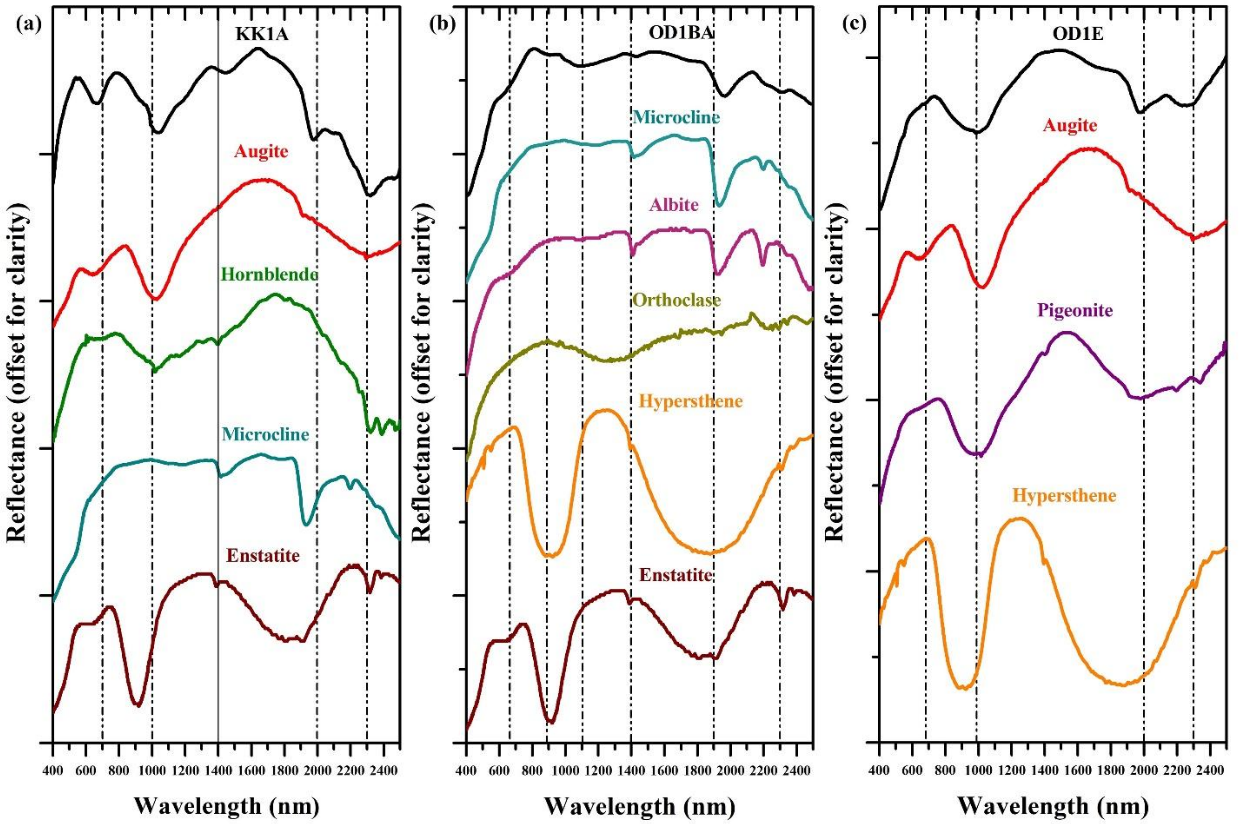

Figure 3 Laboratory reflectance spectra of charnockite samples (a) KK1A, (b) OD1BA and (c) OD1E in the VNIR region are matched with the reference mineral spectra from the USGS spectral library.

In the VNIR region, the spectral behaviour of charnockite samples is dominated by mafic mineralogy (pyroxene and feldspar) since quartz does not show any diagnostic spectral characteristics in the VNIR region. In the VNIR region, KK1A, OD1E, and OD1BA reflectance spectra exhibit diagnostic absorption at nearly 650-700 nm (Figure 3). The absorption features around 700 nm are likely due to the inter-valence charge transfer of Fe^{2+}–Ti^{4+} and Fe^{2+}–Fe^{3+} (Burn, 1993; Clark, 1999). The broad and conspicuous absorption near 1000 nm obtained in KK1A and OD1E is due to the presence of augite, enstatite and hypersthene. OD1BA shows subdued absorption near 900 nm compared to KK1A and ODlE, possibly due to the low abundance of pyroxene. The reflectance spectrum of OD1BA exhibits high reflectance compared to the spectra of KK1A and OD1E. This could be attributed to the presence of feldspar minerals, as they exhibit high reflectance in the VNIR region (Cloutis and Gaffey, 1991; Nair and Mathew, 2014). The feldspar mineral exhibits absorption near 1250 nm due to the small amount of Fe^{2+}. However, the

absorption feature is surpassed by the presence of mafic minerals (Cloutis and Gaffey, 1991). Therefore, charnockite shows spectral absorptions similar to mafic minerals in the VNIR region.
Moreover, The emissivity spectrum of KK1A displays emissivity minima (reststrahlen band) nearly at 8.5 µm, 9.01 µm, and 10.37 µm, which closely matched with reference spectra of quartz, diopside, hypersthene and bytownite (Figure 4a). OD1BA emissivity spectrum exhibits emissivity minima nearly at 8.5 µm, 8.8 µm, 9.3 µm, doublet at 12.52 µm and 12.84 µm, closely matched with the emissivity minima of reference spectra of quartz, oligoclase, hypersthene and enstatite (Figure 4b). OD1E emissivity spectrum shows emissivity minima nearly at 8.54 µm, 9.05 µm, doublets at 10.4 µm and 10.67 µm, 11.20 µm, closely matched with reference spectra of augite, hypersthene, quartz, and bytownite (Figure 4c).

Charnockite spectra show emissivity minima nearly at 8.5 µm, 9 µm, and between 10.5-11 µm, suggesting quartz, felsic and mafic mineralogy. However, the charnockite sample (OD1BA) exhibits low emissivity, nearly at 8.5 and 9 µm and weak absorption near 10 µm, suggesting the presence of quartz and felsic minerals. The KK1A and OD1E exhibit absorption at 8.5 µm, though not as prominent as compared to OD1BA. KK1A and OD1E both show mafic mineral constituents in the TIR region. Therefore, charnockite spectra exhibit the diagnostic absorption of quartz, felsic and mafic minerals in the TIR region.

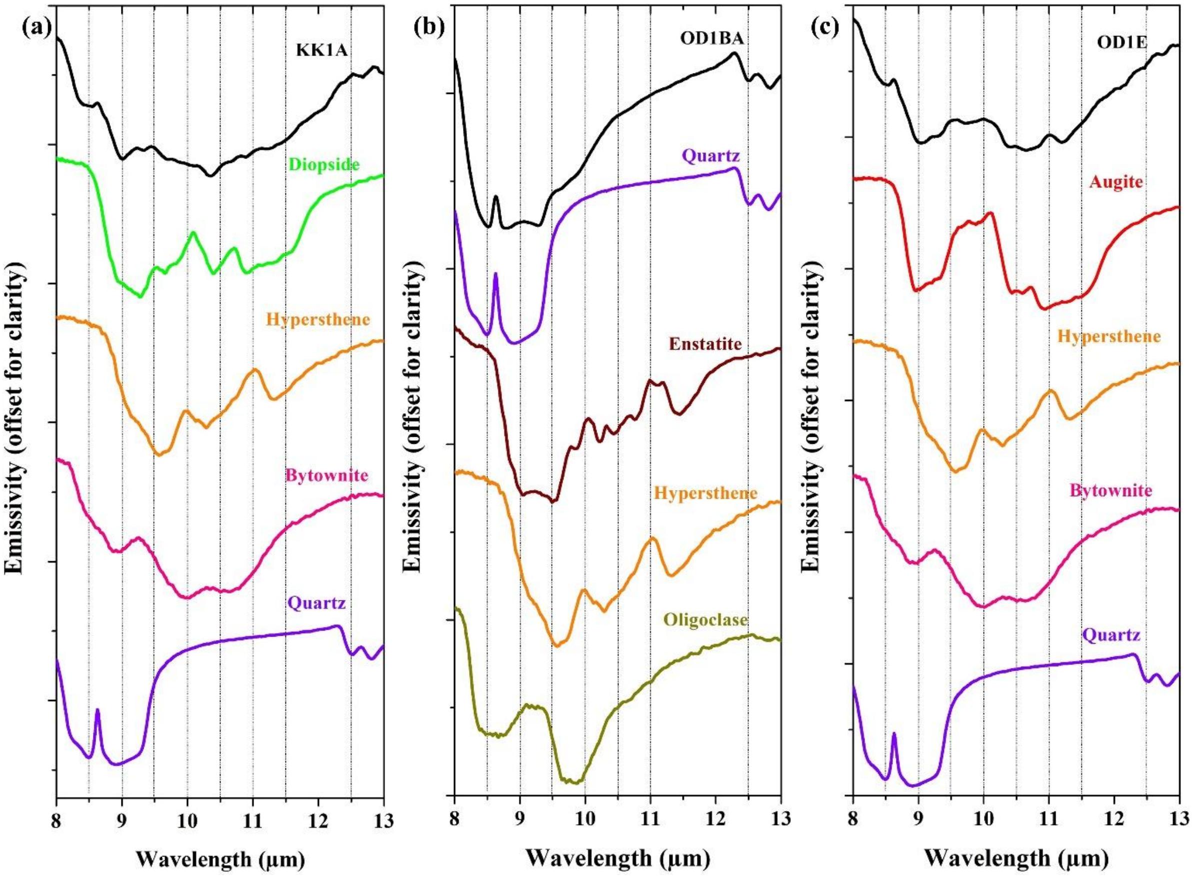

Figure 4 Laboratory emissivity spectra of charnockite samples: (a) KK1A, (b) OD1BA, and (c) OD1E in the TIR region are matched with the reference mineral spectra from ASU spectral library.

3.2 Charnockite on Hellas Basin

The spectral analysis of laboratory spectra of charnockite samples suggests that they exhibit absorption features similar to mafic rocks in the VNIR region. In the TIR region, charnockites exhibit low emissivity features similar to felsic rocks with diagnostic emissivity minima near 8.5 μm of quartz. THEMIS DCS RGB composite images and MAF browse products were used to identify the potential regions showing the coexistence of high mafic and quartz content (refer to Texts S2 and S3 for detailed surface mineralogy). Spectral data were extracted from various locations identified from the THEMIS (SP1T to SP16T) and the CRISM (SP1 to SP16) images, showing the coexistence of quartz and mafic minerals (Figure 5). The THEMIS spectra were selected such that any of the DCS RGB composites — 8-7-5 (Figure 5), 9-6-4 (Figure S8), and 6-4-2 (Figure S9) — showed evidence of quartz or areas displaying a mixture of mafic and quartz regions. Similarly, spectra from CRISM images were extracted from regions indicating the presence of mafic minerals. Emissivity and CRISM ratioed I/F spectra from all those coexisting locations extracted from THEMIS and CRISM MTRDR datasets are given in the supplementary Tables S2 and S4. In addition, statistics of the THEMIS image-derived spectra (SP1T to SP16T), including maximum, minimum, and standard deviation (Stdev) values are given in Table S6(a-o).

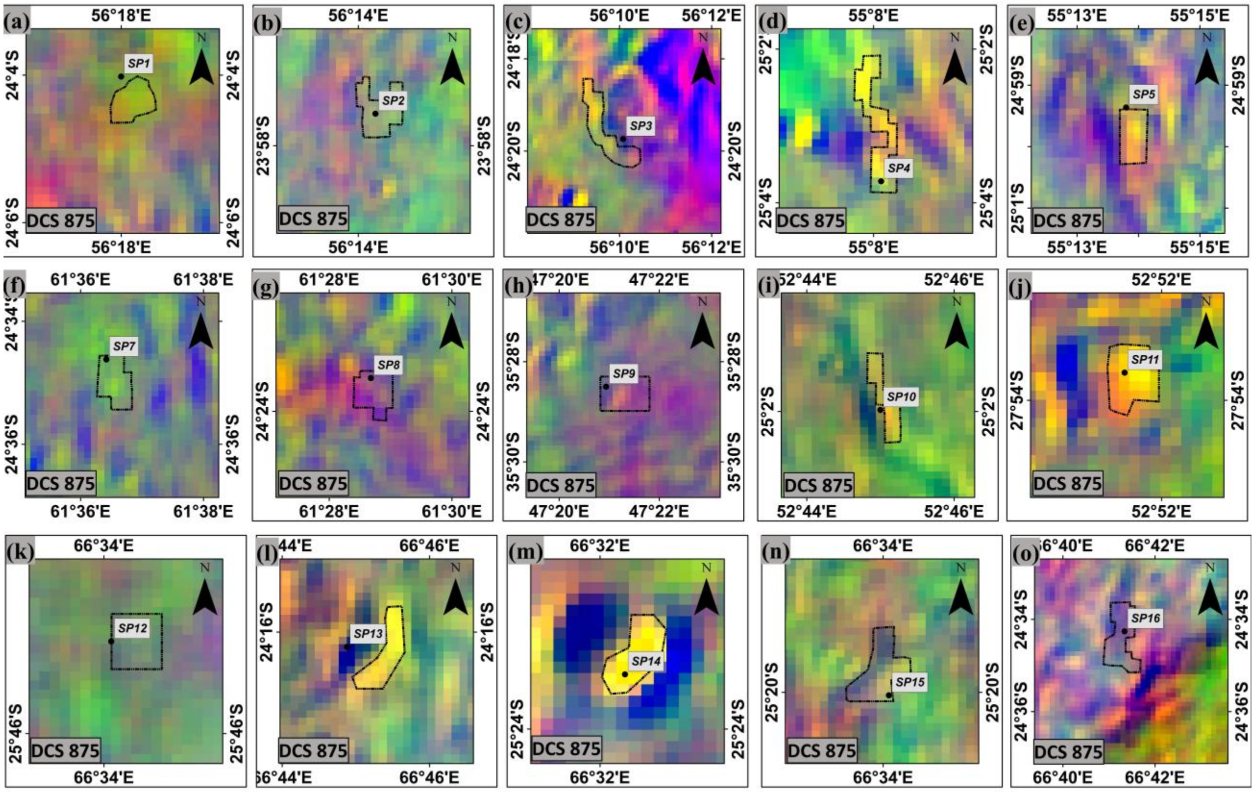

Figure 5 Locations of extracted spectra (SP1 to SP16) from THEMIS and CRISM images. Black boxes mark the Regions of Interest (ROIs) in the THEMIS images, while black dots indicate spectral points extracted from CRISM images. The background shows zoomed-in THEMIS DCS 8-7-5RGB composites.

3.3 Spectral Analysis of THEMIS and CRISM Images

The emissivity spectra from locations SP2T, SP3T, SP5T, and SP8T from THEMIS image show emissivity minima at 8.56, 9.35, and 11.04 μm, closely matched with the emissivity spectra of quartz, diopside, augite, and olivine (Figure 6a). The emissivity spectra from locations SP2T, SP3T, SP5T, and SP8T show spectral similarities with the emissivity spectra of OD1BA and OD1E (Figure 6d). The emissivity spectra from SP1T, SP4T, and SP10T exhibit low emissivity absorption features with band centres at 8.56, 9.35, and 11.04 μm (Figure 6b). However, the SP1T, SP4T, and SP10T spectra show subdued absorption at 11.04 μm (Figure 6b). These emissivity spectra are closely matched with quartz, diopside, and augite (Figure 6b). Further, the emissivity spectra from SP1T, SP4T, and SP10T closely resemble the absorption features observed in the emissivity spectra of charnockite samples, specifically OD1E and OD1BA (Figure 6e). The SP9T emissivity spectrum shows low emissivity minima at 9.35 μm, closely matched with the microcline (Figure 6b). The SP9T emissivity spectrum shows spectral characteristics similar to the emissivity spectrum OD1BA sample of the charnockite (Figure 6e). The emissivity spectra SP7T, SP11T, SP12T, SP13T, SP14T, SP15T and SP16T show spectral similarities to albite, enstatite, labradorite, microcline and quartz with emissivity minima with band centres at 8.56, 9.35 and 10.21 μm (Figure 6c). The SP7T, SP11T, SP12T, SP13T, SP14T, SP15T and SP16T emissivity spectra show spectral characteristics similar to the emissivity spectra of KK1A and OD1BA (Figure 6f).

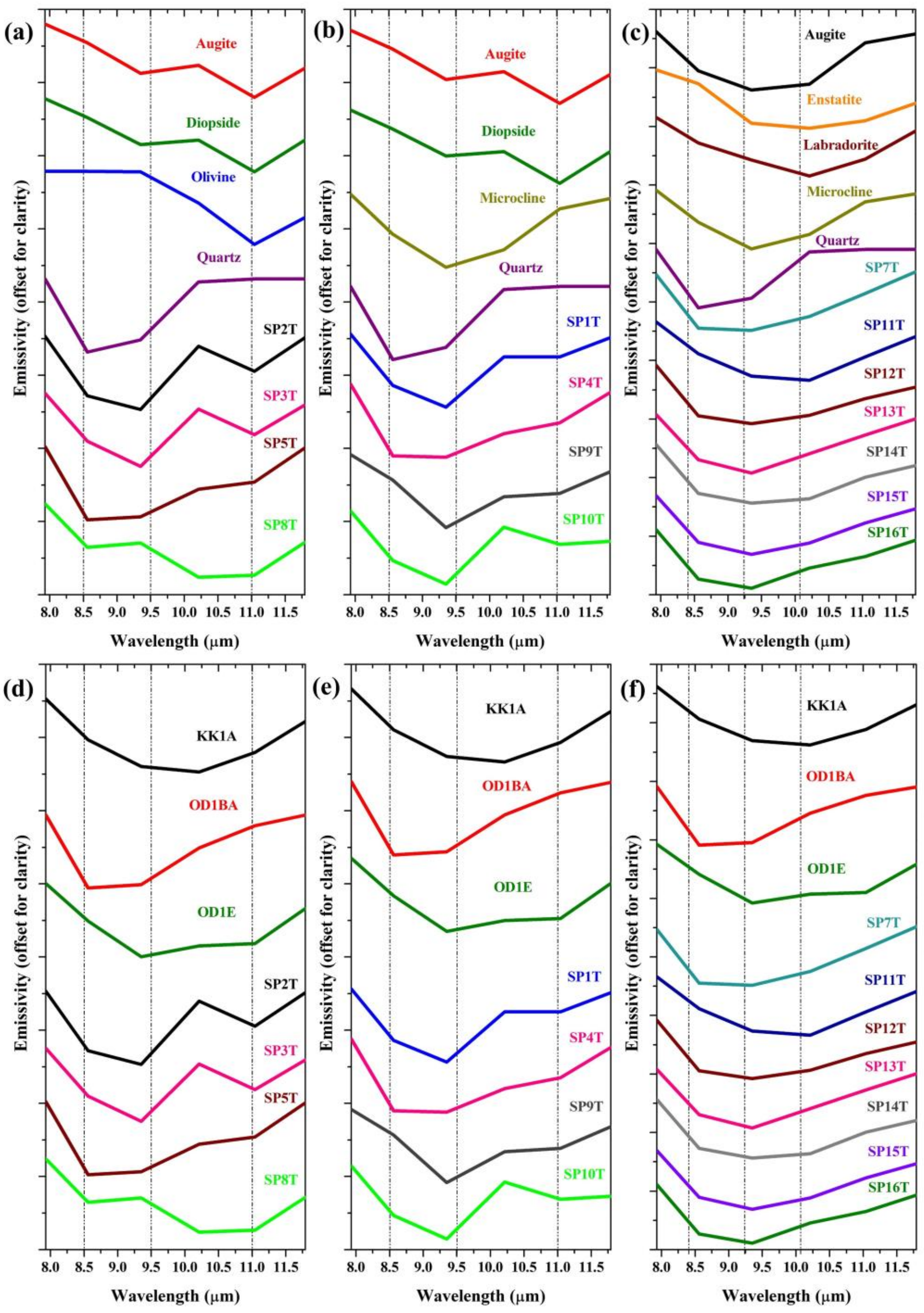

Figure 6 THEMIS image-derived emissivity spectra (SP1T to SP16T) plotted (a,b,c) with reference mineral spectra from ASU spectral library and (d,e,f) with the lab derived emissivity spectra of charnockite samples.

Further, spectra were extracted from the CRISM images for all the locations that demonstrated the presence of quartz and feldspar in the TIR emissivity spectra (Figure 5). The reflectance spectra from SP1 and SP13 exhibit spectral similarities with plagioclase, characterised by broad absorption features with band center nearly at 1300 nm, though this feature is less prominent in the SP1 spectrum (Figure 7a). Additionally, SP1 and SP13 display an absorption feature around 700 nm, which could be attributed to the inter-valence charge transfer of Fe^{2+}–Fe^{3+} (Burn, 1993; Clark, 1999). The reflectance spectra from SP2, SP7, and SP15 show spectral similarity to LCP, HCP, and hematite, with distinct broad absorptions centered around 1000 nm and 2000 nm (Figure 7a). Meanwhile, the reflectance spectra from SP3, SP4, SP5, SP6, SP9, SP12, and SP14 display broad but less pronounced absorption features, with a band center near 1000 nm and subdued absorption around 2000 nm, closely matched with LCP and HCP (Figure 7b). The SP8 spectrum closely corresponds to Mg-olivine and pyroxene, with a broad absorption feature near 1000 nm. Furthermore, SP8 shows a prominent absorption centered around 2200 nm, matching closely with the HCP spectrum (Figure 7c). The SP10 spectrum shows a broad absorption feature with a band center around 1300 nm, aligning closely with plagioclase. The SP11 spectrum displays absorption features near 700 nm and 1000 nm, consistent with HCP, although the absorption feature around 2200 nm is less distinct. Similarly, SP16 shows spectral resemblance to plagioclase, with a broad absorption centered near 1300 nm (Figure 7c). Additionally, SP16 shows broad absorption near 2000 nm, potentially indicating the presence of LCP.

Furthermore, CRISM image-derived reflectance spectra were matched with the laboratory derived charnockite samples, *i.e.*, KK1A, OD1BA and OD1E reflectance spectra (Figure 7 (d,e,f)). The SP1 and SP13 spectra exhibit spectral similarities to the charnockite samples OD1BA. Likewise, the SP2, SP7 and SP15 reflectance spectra show spectral characteristics similar to the charnockite samples KK1A and OD1E (Figure 7d). The reflectance spectra from SP3, SP6, SP9, and SP14 matched closely with KK1A and OD1E, while SP4, SP5, and SP12 match the spectral characteristics of OD1BA and OD1E (Figure 7e). Additionally, the SP10 and SP11 spectra resemble the spectral behavior of OD1BA (Figure 7f). The SP16 spectrum also closely matches the laboratory-derived spectra of OD1BA and OD1E (Figure 7f). Hence, the spectral characteristics of locations co-located from THEMIS and CRISM data indicate the presence of quartz, feldspar, and pyroxene, minerals characteristic of charnockites.

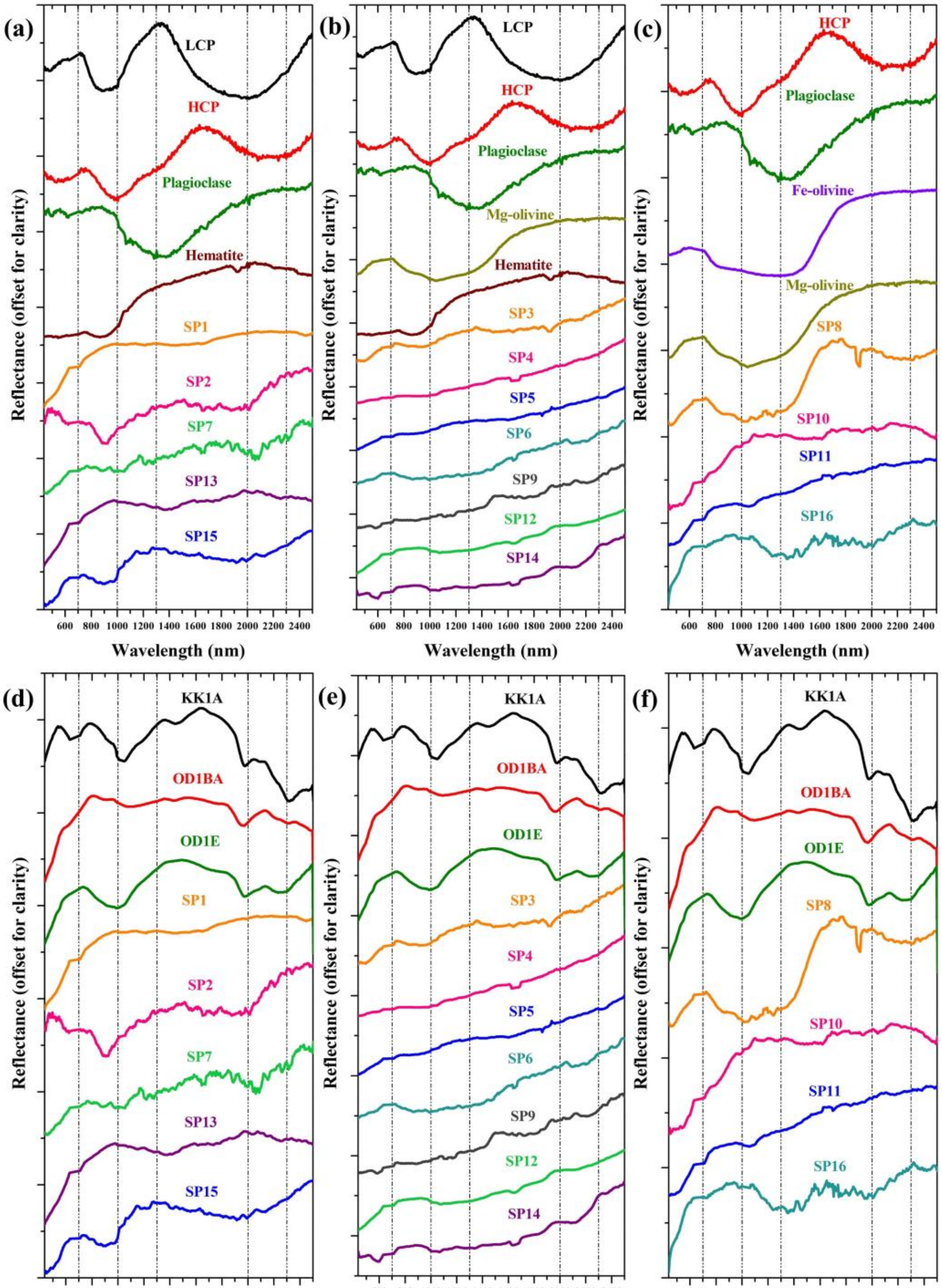

Figure 7 CRISM image-derived ratioed I/F target spectra (SP1 to SP16) plotted (a,b,c) with reference mineral spectra from MICA spectral library and (d,e,f) with the lab reflectance spectra of charnockite samples.

3.4 Spectral Mixture Analysis

The THEMIS image-derived emissivity spectra were deconvolved into their mineral constituents using LMM (Figure S10) for spectra obtained from co-located points in THEMIS and CRISM. Emissivity spectra of albite, augite, enstatite, labradorite, microcline, and quartz from the ASU spectral library resampled to THEMIS band centres were used for deconvolution in the TIR region. The linear deconvolution of SP1T and SP9T emissivity spectra indicates that the spectra consist of a mixture of augite, microcline, and quartz. However, SP9T exhibits a lower abundance of quartz (Figure 8). A high abundance of augite and quartz, along with a low abundance of enstatite, is identified in the LMM for SP2T, SP3T, and SP10T emissivity spectra. Additionally, the LMM of SP3T shows a low abundance of microcline (Figure 8). The SP4T, SP13T, SP15T, and SP16T emissivity spectra suggest that the spectra contain mixtures of albite, enstatite, labradorite, and quartz. However, a low abundance of labradorite is obatined in SP13T, SP15T, and SP16T, while SP4T exhibits a low abundance of enstatite (Figure 8). The SP5T and SP7T emissivity spectra show that the spectra comprise a mixture of albite, labradorite, and quartz (Figure 8). The SP8T spectrum exhibits a high abundance of augite, enstatite, and labradorite. Similarly, SP11T displays a high abundance of albite, enstatite, and labradorite. However, the LMM of SP8T and SP11T spectra show no presence of quartz (Figure 8). Likewise, the SP12T and SP14T spectra show a high abundance of augite and enstatite, with a low abundance of quartz (Figure 8).

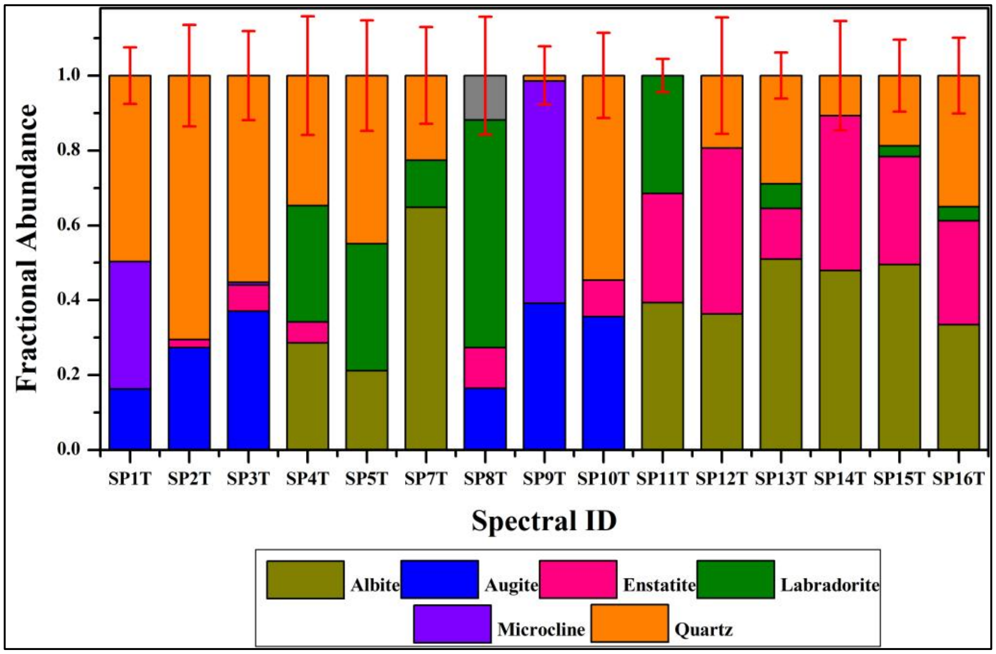

Figure 8 Fractional abundance of minerals and their RMSE obtained from linear deconvolution of THEMIS image-derived emissivity spectra in the TIR region.

Subsequently, the reflectance spectra from the CRISM datasets were deconvolved into their mineral constituents using the PPNM model (Figure S11). For deconvolution in the VNIR region, reflectance spectra of LCP, HCP, plagioclase, hydrated silica, and haematite from the MICA spectral library were used. The CRISM reflectance spectra from SP1, SP7, SP11, SP13, and SP16 indicate the presence of HCP, LCP, plagioclase, and haematite. However, SP1, SP11, and SP13 exhibit a lower abundance of HCP in the PPNM model (Figure 9). The SP2 spectrum is modelled as a mixture of LCP, plagioclase, haematite, and hydrated silica. The abundances of LCP, plagioclase, and haematite are identified in SP3, SP5, SP10, SP12, and SP15 spectra, though SP12 shows a relatively lower abundance of LCP (Figure 9). The PPNM model also identifies plagioclase and haematite, along with a low abundance of hydrated silica, in the SP4, SP6, and SP14 spectra (Figure 9). The SP8 spectrum shows a high abundance of HCP, plagioclase, and haematite, with comparatively lower hydrated silica. For SP9, the model indicates the presence of plagioclase and haematite. Additionally, SP4, SP5, SP9, SP12, SP14, and SP16 exhibit a high abundance of plagioclase (Figure 9). However, the spectra from SP1, SP4, SP6, SP8, SP9, SP10, SP13, SP14, and SP16 were not effectively reconstructed or modelled using the PPNM method, resulting in high RMSE values (Figure 9). These high RMSE values may be attributed either to the limited number of mafic mineral reference spectra in the MICA spectral library or to noise in the CRISM spectra. The results from the spectral characterisation of CRISM image-derived spectra indicate diagnostic absorption features of HCP, LCP, plagioclase, and haematite. Nevertheless, the PPNM model could not identify HCP and LCP in the SP4, SP6, SP9, and SP14 spectra, despite spectral characterisation suggesting the presence of pyroxene-related diagnostic absorption features in these spectra. Therefore, the detection of these minerals implies the possible occurrence of charnockitic rocks in the northern region of the Noachian-aged Hellas basin.

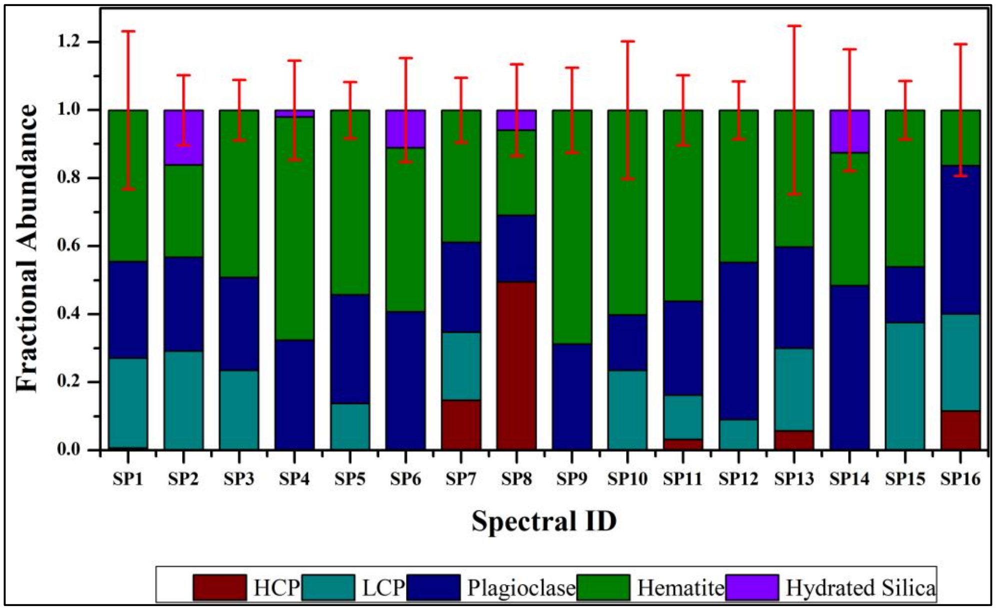

Figure 9 Fractional abundance of minerals and their RMSE obtained from the PPNM model of CRISM image-derived reflectance spectra in the VNIR region.

3.5 Discussion

In this study, the spectral characteristics of charnockites were applied to detect its probable occurrence in the Northern region of the Noachian-aged Hellas basin, Mars. The THEMIS image in the TIR region and the CRISM image in the VNIR region were used to identify the locations showing the coexistence of spectral characteristics of quartz and mafic minerals such as pyroxenes. The DCS (8-7-5, 9-6-4, 6-4-2) images of THEMIS datasets in TIR regions suggested that the northern region of the Hellas basin is characterised by high silica or quartz content. Further, the MAF browse products suggested the presence of mafic minerals. The spectral analysis of the respective spectrum from the THEMIS and the CRISM datasets indicated the presence of quartz, felsic, and mafic minerals. The LMM in the TIR region and the PPNM model in VNIR modelled a considerable concentration of quartz, HCP, LCP, and feldspar for several locations in the Hellas basin. Overall, the results obtained from spectral characterisation and spectral mixture analysis of THEMIS and CRISM datasets suggest the coexistence of mafic and quartz in several regions in the Hellas basins (Figure 10). Also, spectral analysis of SP4, and SP9 show the presence of plagioclase feldspar in the region. The association of these minerals suggests the possible existence of charnockitic rocks on the Martian surface.

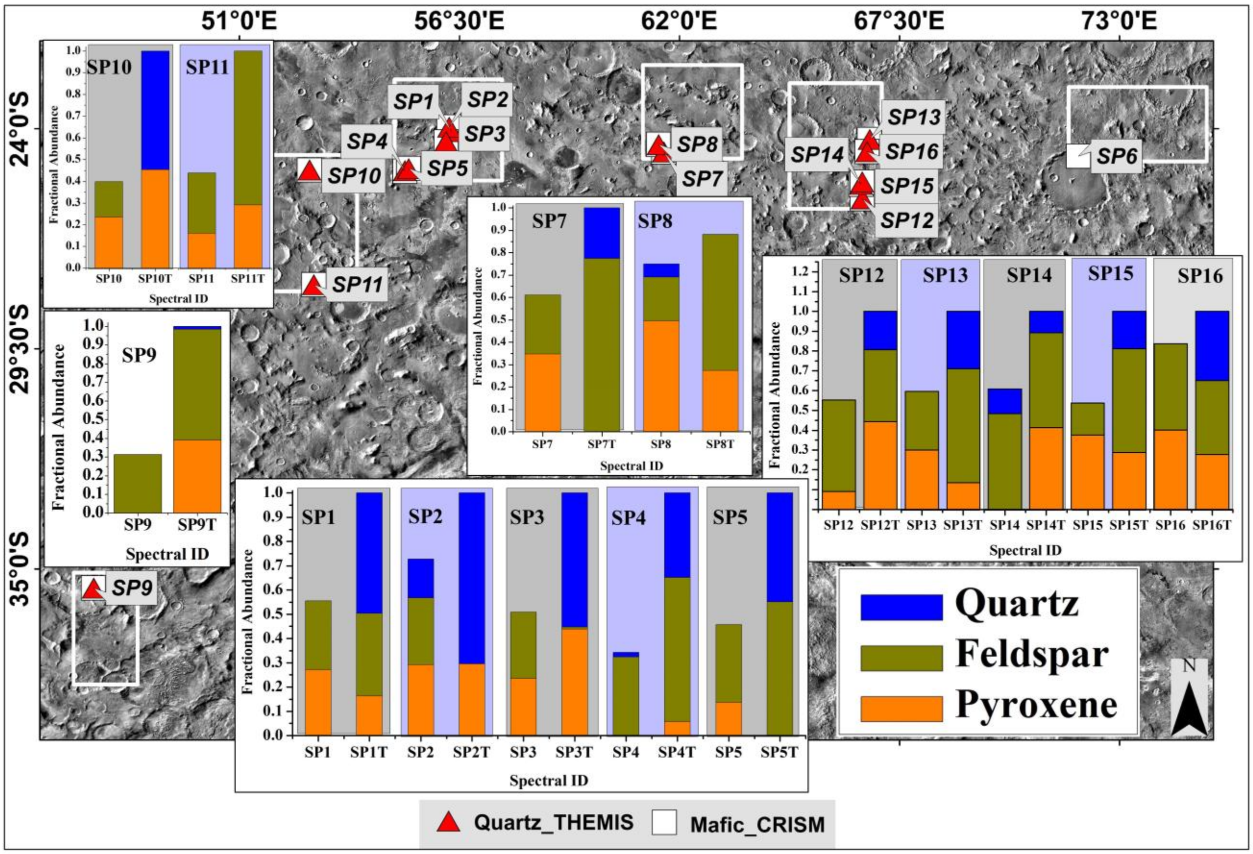

Figure 10 Locations exhibiting a spectrally high abundance of quartz, feldspar and pyroxene mineral overlaid on the THEMIS (visible region) image of the Hellas basin, in inset fractional mineral abundance obtained using LMM (SP1T to SP16T) in the TIR region and PPNM model (SP1 to SP16) in the VNIR region.

Bandfield et al. (2013) reported the presence of hydrated silica in the western Hellas Basin and suggested a direct precipitation mechanism for its formation. Similarly, Carter and Poulet (2013) have identified anorthosite at a few locations of the Hellas basin and suggested the formation originated from magmatic processes. However, later studies identified that feldspar-bearing material in the Hellas basin originated from intermediate and basaltic melts (Rogers and Nekvasil, 2015; Phillips et al., 2022). The Curiosity rover on the Gale Crater has identified the light-toned feldspar-rich magmatic rocks, which indicates a continental crust on early Mars similar to Earth (Sautter et al., 2015).

The charnockite associated with the AMCG suites is formed from direct differentiation of tholeiitic melts with little crustal component or due to ferroan magmatism (Frost and Frost, 2008). Rajesh and Santosh (2004) suggested two stages in the formation of charnockite: the initial stage of basalt underplating and the ponding of alkaline mafic magmas. According to their model, charnockitic magmas were formed by partial melting of this mafic lower crust on Earth. The basalt emplacement with a low water content would cause dehydration melting of the lower crust, resulting in the formation of intermediate charnockites. In contrast, the emplacement of hydrous basalt would increase fH2O melting, leading to more siliceous felsic charnockites (Rajesh and Santosh, 2004). Several studies suggest metamorphism by dehydration through CO_2 influx as a possible mechanism of Charnockite formation (Santhosh et al., 1991). The formation of charnockite on Mars could be either by rift-related ferroan magmatism or partial melting of the mafic crust. Partial melting of mafic crust with low water content and high atmospheric carbon dioxide is a possible scenario for the occurrence of charnockite in Hellas Basin.

4 Conclusions

In this study, the existence of the charnockitic rocks has been postulated in the northern rim of the Hellas basins using THEMIS and CRISM datasets. The laboratory based spectral characteristics of charnockites were utilised to detect its possible occurrence on the Noachian-aged Hellas basin of Mars. THEMIS in the TIR region and CRISM in the VNIR region were used to identify the coexisting location of quartz and mafic minerals. For this purpose, DCS band (8-7-5; 9-6-4; 6-4-2) images from THEMIS datasets were used to obtain the spatial distribution of quartz and high-silica content. Whereas MAF browse products from CRISM MTRDR datasets were used to obtain the spatial distribution of mafic minerals such as olivine, LCP, and HCP. Further, emissivity and reflectance spectra from both THEMIS and CRISM images were extracted from potential locations, showing the coexistence of quartz and mafic minerals in abundance.

Consequently, these spectra were characterised and deconvolved into their mineral constituents using LMM in the TIR region and the PPNM model in the VNIR region. The spectral analysis of emissivity spectra (SP1 to SP16) shows the presence of quartz, felsic and mafic minerals. The reflectance spectra from the same locations show the presence of HCP, LCP, and plagioclase feldspar. The linear deconvolution of emissivity spectra from the northern Hellas basin region shows the high abundance of quartz. The high abundances of LCP, HCP, and feldspar at the exact location of the Hellas basin were obtained using the PPNM model. The assemblage of these minerals at a particular location suggests the presence of the charnockitic rocks. The occurrence of charnockitic rocks on the Noachian-aged Hellas basin suggests active magmatism and crustal differentiation in ancient Mars. Therefore, mapping rocks of charnockite type through remote sensing for terrestrial and planetary exploration requires a combined analysis of VNIR and TIR regions.

Acknowledgements

AA and AMN express their gratitude to IIT Guwahati for the facility and support given during the project. SERB, DST, India funds this project under the scheme Core Research Grant. TJK and ADJ acknowledge Director NCESS for the support.

Open Research

THEMIS (Thermal Emission and Imaging Spectrometer) datasets onboard Mars Odyssey are available at: https://pds-geosciences.wustl.edu/missions/odyssey/themis.html. THEMIS Data Node's Mars Image Explorer at Arizona State University (ASU) allows searches and visualisation of THEMIS data (https://viewer.mars.asu.edu/viewer/themis#T=0). TES atmospheric-corrected emissivity were obtained from ASU TES data tools (http://tes.asu.edu/data_tool/). CRISM (Compact Reconnaissance Imaging Spectrometer for Mars) datasets onboard Mars Reconnaissance Orbiter are available at https://pds-geosciences.wustl.edu/missions/mro/crism.htm. Mars Orbital Data Explorer-Online service that provides search, display, and download tools for CRISM data, developed by the PDS Geosciences Node. The code used for this study was written using MATLAB R2020b software.

References

Adams, J. B. (1974). Interpretation of visible and near-infrared diffuse reflectance spectra of pyroxenes and other rock-forming minerals. *Infrared and Raman spectroscopy of lunar and terrestrial minerals*, 91-116. https://doi.org/10.1029/JB079i032p04829.

Ahmad, A., Kallukalam, T. J., & Nair, A. M. (2020, March). A comparative study of charnockite rocks based on spectroscopic and mineralogical analysis. *In 51st Annual Lunar and Planetary Science Conference* (No. 2326, p. 2059).

Ahmad, A., Patel, R., Deka, B., Nagori, R., Arya, A. S., & Nair, A. M. (2022). Occurrence of Secondary Minerals at Tharsis Montes of Mars: A Critical Assessment, *Icarus*, *378*, 114953. https://doi.org/10.1016/j.icarus.2022.114953.

Ahmad, A., & Nair, A. M. (2024a). Lithological mapping of charnockites using spectral mixture analysis. *Remote Sensing Applications: Society and Environment*, *34*, 101165. https://doi.org/10.1016/j.rsase.2024.101165.

Ahmad, A., & Nair, A. M. (2024b). Spectral mixture analysis of intimate mixtures for lithological mapping. *ISPRS Journal of Photogrammetry and Remote Sensing*, *208*, 210-232. https://doi.org/10.1016/j.isprsjprs.2023.12.014.

Altmann, Y., Halimi, A., Dobigeon, N., & Tourneret, J. Y. (2012). Supervised nonlinear spectral unmixing using a postnonlinear mixing model for hyperspectral imagery. *IEEE Transactions on Image Processing*, *21*(6), 3017-3025. https://doi.org/10.1109/TIP.2012.2187668.

Bandfield, J. L. (2002). Global mineral distributions on Mars. *Journal of Geophysical Research: Planets*, *107*(E6), 9-1. https://doi.org/10.1029/2001JE001510.

Bandfield, J. L., Rogers, D., Smith, M. D., & Christensen, P. R. (2004). Atmospheric correction and surface spectral unit mapping using Thermal Emission Imaging System data. *Journal of Geophysical Research: Planets*, *109*(E10). https://doi.org/10.1029/2004JE002289.

Bandfield, J. L. (2006). Extended surface exposures of granitoid compositions in Syrtis Major, Mars. *Geophysical research letters*, *33*(6). https://doi.org/10.1029/2005GL025559.

Bandfield, J. L., Amador, E. S., & Thomas, N. H. (2013). Extensive hydrated silica materials in western Hellas Basin, Mars. *Icarus*, *226*(2), 1489-1498. https://doi.org/10.1016/j.icarus.2013.08.005.

Bioucas-Dias, J. M., Plaza, A., Dobigeon, N., Parente, M., Du, Q., Gader, P., & Chanussot, J. (2012). Hyperspectral unmixing overview: Geometrical, statistical, and sparse regression-based approaches. *IEEE journal of Selected Topics in Applied Earth Observations and Remote Sensing*, *5*(2), 354-379. https://doi.org/10.1109/JSTARS.2012.2194696.

Brandt, S., Raith, M. M., Schenk, V., Sengupta, P., Srikantappa, C., & Gerdes, A. (2014). Crustal evolution of the Southern Granulite Terrane, south India: New geochronological and geochemical data for felsic orthogneisses and granites. *Precambrian Research, 246*, 91-122. https://doi.org/10.1016/j.precamres.2014.01.007.

Burns, R. (1993). Mineralogical Applications of Crystal Field Theory, Second Edition, Cambridge University Press, Cambridge, 551p.

Carter, J., & Poulet, F. (2013). Ancient plutonic processes on Mars inferred from the detection of possible anorthositic terrains. *Nature Geoscience*, *6*(12), 1008-1012. https://doi.org/10.1038/ngeo1995.

Catlos, E.J., Sayit, K., Sivasubramanian, P., & Dubey, C.S. (2011). Geochemical and geochronological data from charnockites and anorthosites from India's Kodaikanal–Palani Massif, Southern granulite terrain, India. *Topics in Igneous Petrology*, pp.383-417. https://doi.org/10.1007/978-90-481-9600-5_15.

Christensen, P. R. et al. (2000). A thermal emission spectral library of rock-forming minerals. *Journal of Geophysical Research: Planets*, *105*(E4), 9735-9739. https://doi.org/10.1029/1998JE000624.

Christensen, P.R. et al. (2001). Mars global surveyor thermal emission spectrometer experiment: investigation description and surface science results. *J. Geophys. Res. 106*, 23,823–23,871. https://doi.org/10.1029/2000JE001370.

Christensen, P.R. et al. (2004). The thermal emission imaging system (THEMIS) for the Mars 2001 odyssey mission. *Space Sci. Rev. 110*, 85–130. https://doi.org/10.1007/978-0-306-48600-5_3.

Clark, C., Collins, A. S., Taylor, R. J., & Hand, M. (2020). Isotopic systematics of zircon indicate an African affinity for the rocks of southernmost India. *Scientific reports*, *10*(1), 5421. https://doi.org/10.1038/s41598-020-62075-y.

Clark, R. N. (1999). Spectroscopy of rocks and minerals, and principles of spectroscopy. *In Remote Sensing for the Earth Sciences (ed. Renez, A. N.), John Wiley, New York 3*, 3–58.

Cloutis, E. A., & Gaffey, M. J. (1991). Pyroxene spectroscopy revisited: Spectral-compositional correlations and relationship to geothermometry. *Journal of Geophysical Research: Planets*, *96*(E5), 22809-22826. https://doi.org/10.1029/91JE02512.

Cousin, A. et al. (2017). Classification of igneous rocks analyzed by ChemCam at Gale crater, Mars. *Icarus*, *288*, 265-283.https://doi.org/10.1016/j.icarus.2017.01.014.

Deka, B., Ahmad, A., Patel, R. R., & Nair, A. M. (2019). Spectral Mapping of the Pavonis Mons of Mars using CRISM and THEMIS data. *AGU Fall Meeting Abstracts*. https://ui.adsabs.harvard.edu/abs/2019AGUFMEP21E2215D/abstract.

Deka, B., Ahmad, A., Patel, R. R., & Nair, A. M. (2020). Spectral Mapping of Tharsis Montes of Mars Using CRISM and THEMIS Data. *In Lunar and Planetary Science Conference 2326*, 1273.

Dev, J. A., Tomson, J. K., Kumar, T. V. & Sorcar, N. (2023). Age and petrogenesis of mafic granulites from central Madurai block, south India: implications on regional tectonics. *Geological Magazine, 160*(5), 955-971. https://doi.org/10.1017/S0016756823000079.

Dobigeon, N., Tourneret, J. Y., Richard, C., Bermudez, J. C. M., McLaughlin, S., & Hero, A. O. (2013). Nonlinear unmixing of hyperspectral images: Models and algorithms. *IEEE Signal processing magazine, 31*(1), 82-94. https://doi.org/10.1109/MSP.2013.2279274.

Ehlmann, B. L. et al., 2011. Subsurface water and clay mineral formation during the early history of Mars. Nature 479, 53–60. https://doi.org/10.1038/nature10582.

Ehlmann, B. L., Bish, D. L., Ruff, S. W., & Mustard, J. F. (2012). Mineralogy and chemistry of altered Icelandic basalts: Application to clay mineral detection and understanding aqueous environments on Mars. *Journal of Geophysical Research: Planets, 117*(E11). https://doi.org/10.1029/2012JE004156.

Frost, B. R., Barnes, C. G., Collins, W. J., Arculus, R. J., Ellis, D. J., & Frost, C. D. (2001). A geochemical classification for granitic rocks. *Journal of petrology, 42*(11), 2033-2048. https://doi.org/10.1093/petrology/42.11.2033.

Frost, B. R., & Frost, C. D. (2008). On charnockites. *Gondwana Research, 13*(1), 30-44. https://doi.org/10.1016/j.gr.2007.07.006.

Gillespie, A. R., Kahle, A. B., & Walker, R. E. (1986). Color enhancement of highly correlated images. I. Decorrelation and HSI contrast stretches. *Remote Sensing of Environment, 20*(3), 209-235. https://doi.org/10.1016/0034-4257(86)90044-1.

Gupta, R. P. (2005). Remote Sensing Geology, 2nd edn. *Springer verlag*, p 627.

Hamilton, V. E., & Christensen, P. R., (2000). Determining the modal mineralogy of mafic and ultramafic igneous rocks using thermal emission spectroscopy. *Journal of Geophysical Research: Planets, 105*(E4), 9717-9733. https://doi.org/10.1029/1999JE001113.

Hamilton, V. E., Wyatt, M. B., McSween Jr, H. Y., & Christensen, P. R. (2001). Analysis of terrestrial and Martian volcanic compositions using thermal emission spectroscopy: 2. Application to Martian surface spectra from the Mars Global Surveyor Thermal Emission Spectrometer. *Journal of Geophysical Research: Planets*, *106*(E7), 14733-14746. https://doi.org/10.1029/2000JE001353.

Hecker, C., van Ruitenbeek, F. J., van der Werff, H. M., Bakker, W. H., Hewson, R. D., & van der Meer, F. D. (2019). Spectral absorption feature analysis for finding ore: A tutorial on using the method in geological remote sensing. *IEEE Geoscience and Remote Sensing Magazine*, *7*(2), 51-71. https://doi.org/10.1109/MGRS.2019.2899193.

Heylen, R., & Gader, P. (2013). Nonlinear spectral unmixing with a linear mixture of intimate mixtures model. *IEEE Geoscience and Remote Sensing Letters*, *11*(7), 1195-1199. https://doi.org/10.1109/LGRS.2013.2288921.

Howie, R. A. (1955). XVIII.—the geochemistry of the charnockite series of Madras, India. *Earth and Environmental Science Transactions of the Royal Society of Edinburgh*, *62*(3), 725-768. https://doi.org/10.1017/S0080456800009431.

Keshava, N., & Mustard, J. F. (2002). Spectral unmixing. *IEEE Signal Processing Magazine*, *19*(1), 44-57. https://doi.org/10.1109/79.974727.

Kokaly, R. F., Clark, R. N., Swayze, G. A., Livo, K. E., Hoefen, T. M., & Benzel, W. M. (2017). USGS spectral library version 7 data. *US Geological Survey data release*. Retrieved from https://dx. doi. org/10.5066/F7RR1WDJ.

Kumar, T. V., Rao, Y. B., Plavsa, D., Collins, A. S., Tomson, J. K., Gopal, B. V., & Babu, E. V. S. S. K. (2017). Zircon U-Pb ages and Hf isotopic systematics of charnockite gneisses from the Ediacaran–Cambrian high-grade metamorphic terranes, southern India: Constraints on crust formation, recycling, and Gondwana correlations. *Bulletin*, *129*(5-6), 625-648. https://doi.org/10.1130/B31474.1.

Leonard, G. J., & Tanaka, K. L. (2001). Geologic map of the Hellas region of Mars. *US Department of the Interior. US Geological Survey*. https://pubs.usgs.gov/imap/i2694/.

Loizeau, D. et al. (2012). Characterization of hydrated silicate-bearing outcrops in Tyrrhena Terra, Mars: Implications to the alteration history of Mars. *Icarus*, *219*(1), 476-497. https://doi.org/10.1016/j.icarus.2012.03.017.

Lyon, R. J. P. (1965). Analysis of rocks by spectral infrared emission (8 to 25 microns). *Economic Geology*, *60*(4), 715-736. https://doi.org/10.2113/gsecongeo.60.4.715.

Mathew, G., Nair, A., Gundu Rao, T. K., & Pande, K. (2009). Laboratory technique for quantitative thermal emissivity measurements of geological samples. *Journal of Earth System Science*, *118*, 391-404. https://doi.org/10.1007/s12040-009-0035-4.

McGuire, P.C. et al. (2009). An improvement to the volcano-scan algorithm for atmospheric correction of CRISM and OMEGA spectral data. *Planetary and Space Science 57*, 809–815 0903.3672. https://doi.org/10.1016/j.pss.2009.03.007.

Milam, K. A., McSween Jr, H. Y., Moersch, J., & Christensen, P. R. (2010). Distribution and variation of plagioclase compositions on Mars. *Journal of Geophysical Research: Planets*, *115*(E9). https://doi.org/10.1029/2009JE003495.

Murchie, S. et al. (2007). Compact Reconnaissance Imaging Spectrometer for Mars (CRISM) on Mars Reconnaissance Orbiter (MRO). *J. Geophys. Res. 112*, E05S03. https://dx.doi.org/10.1029/2006JE002682.

Murchie, S.L. et al. (2009). A synthesis of Martian aqueous mineralogy after 1 Mars year of observations from the Mars Reconnaissance Orbiter. *J. Geophys. Res. 114*. https://doi.org/10.1029/2009JE003342.

Mustard, J. F. et al. (2005). Olivine and pyroxene diversity in the crust of Mars. *Science*, *307*(5715), 1594-1597. https://doi.org/10.1126/science.1109098.

Nair, A. M., & Mathew, G. (2014). Effect of bulk chemistry in the spectral variability of igneous rocks in VIS-NIR region: Implications to remote compositional mapping. International *Journal of Applied Earth Observation and Geoinformation*, *30*, 227-237. https://doi.org/10.1016/j.jag.2014.02.004.

Nair, A. M., & Mathew, G. (2017). Geochemical modelling of terrestrial igneous rock compositions using laboratory thermal emission spectroscopy with an overview on its applications to Indian Mars Mission. *Planetary and Space Science*, *140*, 62-73. https://doi.org/10.1016/j.pss.2017.04.009.

Payré, V., Salvatore, M. R., & Edwards, C. S. (2022). An evolved early crust exposed on Mars revealed through spectroscopy. *Geophysical research letters*, *49*(21), e2022GL099639. https://doi.org/10.1029/2022GL099639.

Phillips, M. S., Viviano, C. E., Moersch, J. E., Rogers, A. D., McSween, H. Y., & Seelos, F. P., (2022). Extensive and ancient feldspathic crust detected across north Hellas rim, Mars: Possible implications for primary crust formation. *Geology, 50*(10), 1182-1186. https://doi.org/10.1130/G50341.1.

Pompilio, L., Sgavetti, M., & Pedrazzi, G. (2007). Visible and near-infrared reflectance spectroscopy of pyroxene-bearing rocks: New constraints for understanding planetary surface compositions. *Journal of Geophysical Research: Planets, 112*(E1). https://doi.org/10.1029/2006JE002737.

Poulet, F. et al. (2009). Quantitative compositional analysis of Martian mafic regions using the MEx/OMEGA reflectance data: 2. Petrological implications. *Icarus, 201*(1), 84-101. https://doi.org/10.1016/j.icarus.2008.12.042.

Poulet, F., & Erard, S. (2004). Nonlinear spectral mixing: Quantitative analysis of laboratory mineral mixtures. *J. Geophys. Res.*, *109*, E02009. https://doi.org/10.1029/2003JE002179.

Rajesh, H. M., & Santosh, M. (2004). Charnockitic magmatism in southern India. *Journal of Earth System Science, 113*, 565-585. https://doi.org/10.1007/BF02704023.

Ramsey, M. S., & Christensen, P. R. (1998). Mineral abundance determination: Quantitative deconvolution of thermal emission spectra. *Journal of Geophysical Research: Solid Earth, 103*(B1), 577-596. https://doi.org/10.1029/97JB02784.

Rogers, A. D., & Christensen, P. R. (2007). Surface mineralogy of Martian low-albedo regions from MGS-TES data: Implications for upper crustal evolution and surface alteration. *Journal of Geophysical Research: Planets*, *112*(E1). https://doi.org/10.1029/2006JE002727.

Rogers, A. D., Aharonson, O., & Bandfield, J. L. (2009). Geologic context of in situ rocky exposures in Mare Serpentis, Mars: Implications for crust and regolith evolution in the cratered highlands. *Icarus, 200*(2), 446-462. https://doi.org/10.1016/j.icarus.2008.11.026.

Rogers, A. D., & Nekvasil, H. (2015). Feldspathic rocks on Mars: Compositional constraints from infrared spectroscopy and possible formation mechanisms. *Geophysical Research Letters, 42*(8), 2619-2626. https://doi.org/10.1002/2015GL063501.

Ruff, S. W., Christensen, P. R., Barbera, P. W., & Anderson, D. L. (1997). Quantitative thermal emission spectroscopy of minerals: A laboratory technique for measurement and calibration. *Journal of Geophysical Research: Solid Earth*, *102*(B7), 14899-14913. https://doi.org/10.1029/97JB00593.

Salisbury, J. W. (1988). Mid-infrared (2.5 to 13.5 μm) spectra of igneous rocks. *US Geological Survey Open-File Report* 88-686. https://doi.org/110.3133/ofr88686.

Salisbury, J. W., Eastes, J. W. (1985). The effect of particle size and porosity on spectral contrast in the mid-infrared. *Icarus*, *64*(3), 586-588. https://doi.org/10.1016/0019-1035(85)90078-8.

Samuel, V. O., Kwon, S., Jang, Y., & Santosh, M. (2020). Petrogenesis of the late Paleoproterozoic Luyashan igneous charnockite-enderbite suite, North China Craton and its comparison with metamorphic counterparts. *Lithos*, *376*, 105724. https://doi.org/10.1016/j.lithos.2020.105724.

Santosh, M., Chao-Nan Hu, Xiao-Fang He, Shan-Shan Li, T. Tsunogae, Shaji., E. & Indu., G. (2017). Neoproterozoic arc magmatism in the southern Madurai block, India: Subduction, relamination, continental outbuilding, and the growth of Gondwana. *Gondwana Research*, *45*, 1-42. https://doi.org/10.1016/j.gr.2016.12.009.

Santosh, M., Jackson, D. H., Harris, N. B. W., & Mattey, D. P. (1991). Carbonic fluid inclusions in South Indian granulites: evidence for entrapment during charnockite formation. *Contributions to Mineralogy and Petrology*, *108*, 318-330. https://doi.org/10.1007/BF00285940.

Santosh, M., Yang, Q. Y., Shaji, E., Tsunogae, T., Mohan, M. R., & Satyanarayanan, M. (2015). An exotic Mesoarchean microcontinent: the Coorg block, southern India. *Gondwana Research*, *27*(1), 165-195. https://doi.org/10.1016/j.gr.2013.10.005.

Sautter, V. et al. (2015). In situ evidence for continental crust on early Mars. *Nature Geoscience*, *8*(8), 605-609. https://doi.org/10.1038/ngeo2474.

Skok, J. R., Mustard, J. F., Tornabene, L. L., Pan, C., Rogers, D., & Murchie, S. L. (2012). A spectroscopic analysis of Martian crater central peaks: Formation of the ancient crust. *Journal of Geophysical Research: Planets*, *117*(E11). https://doi.org/10.1029/2012JE004148.

Tanaka, K. L., & Leonard, G. J. (1995). Geology and landscape evolution of the Hellas region of Mars. *Journal of Geophysical Research: Planets*, *100*(E3), 5407-5432. https://doi.org/10.1029/94JE02804.

Tanaka, K. L., Robbins, S. J., Fortezzo, C. M., Skinner Jr, J. A., & Hare, T. M. (2014). The digital global geologic map of Mars: Chronostratigraphic ages, topographic and crater morphologic characteristics, and updated resurfacing history. *Planetary and Space Science, 95*, 11-24. https://doi.org/10.1016/j.pss.2013.03.006.

Tomson, J. K., & Dev, J. A. (2023). Tracing the crustal evolution of the Precambrian Southern Granulite terrane in East Gondwana: New insights from zircon U-Pb/Hf geochronology. *GSA Bulletin*. https://doi.org/10.1130/B36777.1.

Tomson, J. K., Rao, Y. B., Kumar, T. V., & Choudhary, A. K. (2013). Geochemistry and neodymium model ages of Precambrian charnockites, Southern Granulite Terrain, India: Constraints on terrain assembly. *Precambrian Research, 227*, 295-315. https://doi.org/10.1016/j.precamres.2012.06.014.

Tomson, J. K., Rao, Y. B., Kumar, T. V., & Rao, J. M. (2006). Charnockite genesis across the Archaean–Proterozoic terrane boundary in the South Indian Granulite Terrain: Constraints from major–trace element geochemistry and Sr–Nd isotopic systematics. *Gondwana Research, 10*(1-2), 115-127. https://doi.org/10.1016/j.gr.2005.11.023.

Touret, J. L., & Huizenga, J. M. (2012). Charnockite microstructures: from magmatic to metamorphic. *Geoscience Frontiers, 3*(6), 745-753. https://doi.org/10.1016/j.gsf.2012.05.004.

van der Werff, H., van Ruitenbeek, F., & van der Meer, F. (2007). Geological mapping on Mars by segmentation of hyperspectral OMEGA data. *In 2007 IEEE International Geoscience and Remote Sensing Symposium, Barcelona, Spain*. 2811-2813. https://doi.org/0.1109/IGARSS.2007.4423427.

Viviano, C. E., & Phillips, M. S. (2019, July). Hydrothermal Alteration Related to Large Impact Basins. *In Ninth International Conference on Mars (Vol. 2089*, p. 6359).

Viviano-Beck, C.E. et al. (2014). Revised CRISM spectral parameters and summary products based on the currently detected mineral diversity on Mars. *J. Geophys. Res. Planets 119*, 1403–1431. https://doi.org/10.1002/2014JE004627.

Wray, J. J. et al. (2013). Prolonged magmatic activity on Mars inferred from the detection of felsic rocks. *Nature Geoscience, 6*(12), 1013-1017. https://doi.org/10.1038/ngeo1994.

Wyatt, M. B., Hamilton, V. E., McSween Jr, H. Y., Christensen, P. R., & Taylor, L. A. (2001). Analysis of terrestrial and Martian volcanic compositions using thermal emission spectroscopy: 1. Determination of mineralogy, chemistry, and classification strategies. *Journal of Geophysical Research: Planets, 106*(E7), 14711-14732. https://doi.org/10.1029/2000JE001356.

Existence of Charnockites in Hellas Basin, Mars

Adnan Ahmad[1], Archana M. Nair[1] J.K Tomson[2] and J. Amal Dev[2]

[1]Earth System Science and Engineering Group, Department of Civil Engineering, Indian Institute of Technology Guwahati, Assam, India

[2]National Centre for Earth Science Studies, Thiruvananthapuram, India

Corresponding author: Archana M. Nair (nair.archana@iitg.ac.in)

Contents of this file

This Supplementary materials document includes:

- Text S1: Spectral Mixture Analysis for Laboratory-derived Spectra
- Text S1: Decorrelation Stretch Images from THEMIS Datasets
- Text S2: Spatial Distribution of Mafic Minerals
- Figures S1 to S10
- Table 5a to 5o

Additional Supporting Information (Files uploaded separately)

Other Supplementary data for this manuscript include the following:

- Table S1 [Detailed information on THEMIS images used in the study]
- Table S2 [Detailed locations of target emissivity spectra from THEMIS images with the averaging windows]
- Table S3 [Detailed information on CRISM images used in the study]
- Table S4 [Detailed locations of target and flat spectra from CRISM images with the averaging windows]
- Table S5 [Detailed spectral parameters (band position, band width, area, and asymmetry) of charnockite samples KK1A, OD1BA and OD1E.]

Introduction

This supporting document provides information on the spectral mixing models used in this study, namely the Linear Mixing Model (LMM) and the Polynomial Post-Nonlinear Model (PPNM), applied to laboratory-derived spectra. It also investigates the spatial distribution of mafic and felsic minerals in the Hellas basin using THEMIS and CRISM datasets. Additionally, the document includes spectral plots, spectral mixing results, and zoomed-in locations of extracted spectra over DCS images.

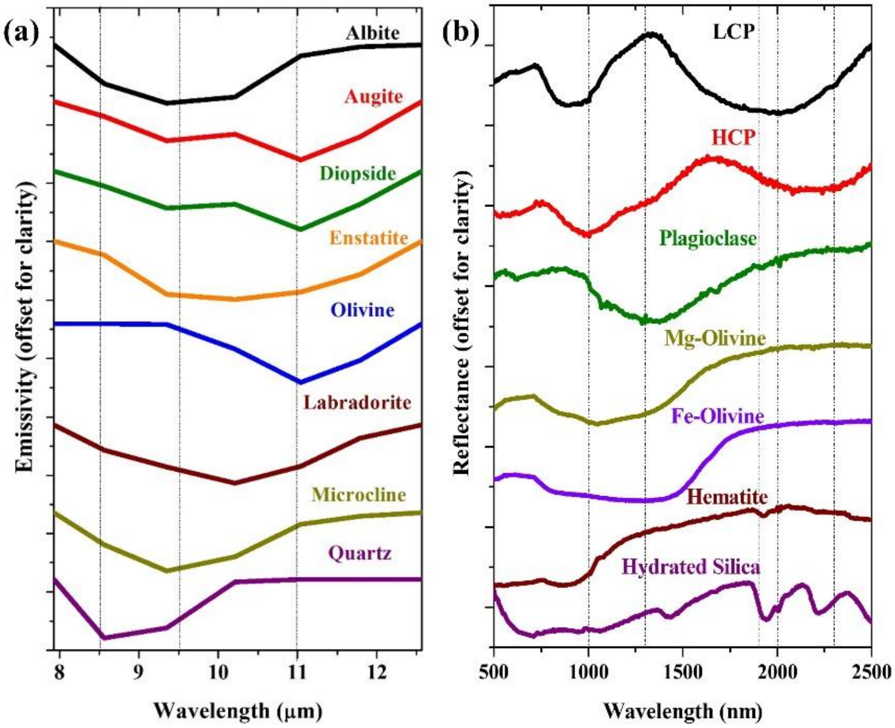

Figure S1 Spectral plots of reference minerals from (a) the ASU spectral library in the TIR region and (b) the MICA spectral library in the VNIR region.

5 Text S1: **Spectral Mixture Analysis for Laboratory-derived Spectra**

Spectral mixture analysis was performed on laboratory-derived spectra to assess the effectiveness of the models. For this purpose, reference spectra from the ASU spectral library in the thermal infrared (TIR) region and the USGS spectral library in the visible-near infrared (VNIR) region were utilised to deconvolve the laboratory-derived charnockite spectra into their mineral constituents. These spectra were further resampled to match the wavelengths corresponding to THEMIS in the TIR region and CRISM in the VNIR region. In the TIR region, the charnockite rock samples were deconvolved into their mineral constituents and corresponding abundances using the Linear Mixing Model (LMM) (Figure S2a-c). The emissivity spectrum of KK1A indicates a combination of albite, enstatite, and labradorite (Figure S3a). The OD1BA spectrum exhibits a mixture of albite, enstatite, labradorite, and quartz (Figure S3a), while OD1E comprises albite and quartz (Figure S3a). Notably, OD1BA and OD1E display quartz abundance, whereas KK1A does not indicate any quartz. The RMSE obtained from the LMM is low across all samples, although OD1E records a relatively higher RMSE compared to KK1A and OD1BA (Figure S3a).

In the VNIR region, the charnockite samples were deconvolved using the Polynomial Post Nonlinear Mixing (PPNM) model to estimate mineral abundances (Figure S2d-f). The reflectance spectrum of KK1A demonstrates a combination of albite, bytownite, hornblende, and pigeonite (Figure S3b). The OD1BA spectrum identifies albite, microcline, labradorite, hypersthene, hornblende, and pigeonite as its constituents (Figure S3b), while OD1E comprises microcline, labradorite, hypersthene, hornblende, augite, pigeonite, and haematite (Figure S3b). The major contributing minerals identified in the charnockite samples are pyroxene and feldspar in the VNIR region, with OD1E showing a low abundance of haematite (Figure S3b). The RMSE obtained from the PPNM model is also low, though KK1A shows a relatively higher RMSE compared to OD1BA and OD1E (Figure S3b). Hence, LMM in the TIR region identified albite, enstatite, labradorite, and quartz, while the PPNM in the VNIR region demonstrated the presence of pyroxenes, feldspars, and haematite. The results highlight the dominance of pyroxene, feldspar and quartz as major contributing minerals, characteristic of charnockitic lithology. The low RMSE values in both models indicate a good fit between the observed and modelled spectra, validating the applicability of these methods for mineralogical analysis.

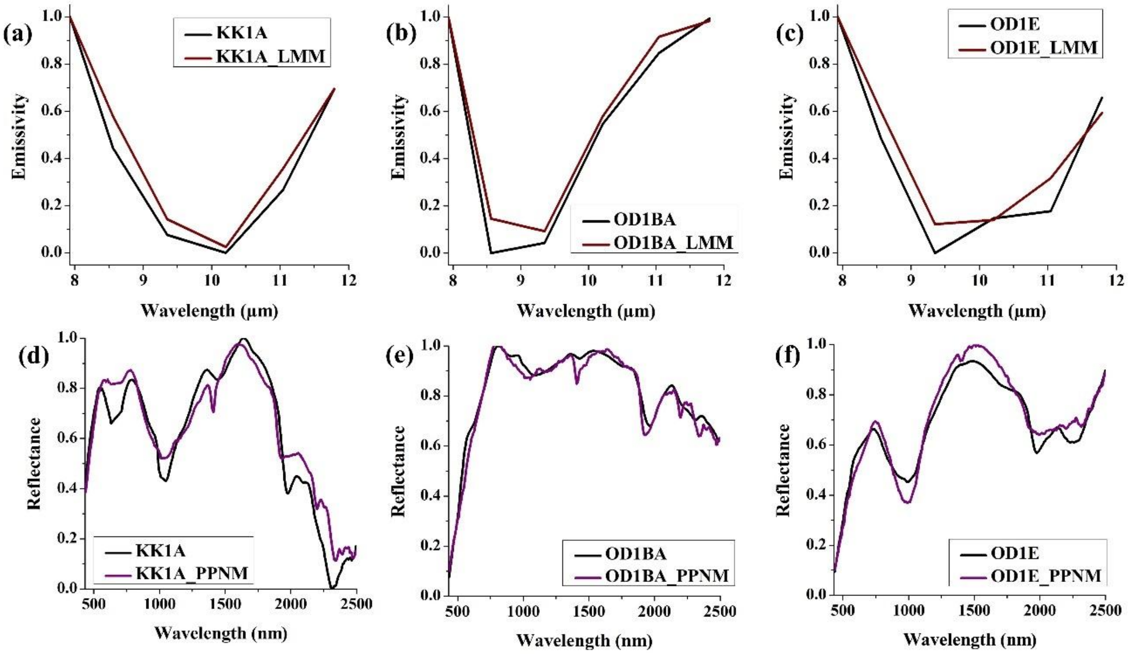

Figure S2 Spectral matching of laboratory-derived and modelled spectra for charnockite rock samples using LMM in the TIR region for (a) KK1A, (b) OD1BA, and (c) OD1E, and using PPNM in the VNIR region for (d) KK1A, (e) OD1BA, and (f) OD1E.

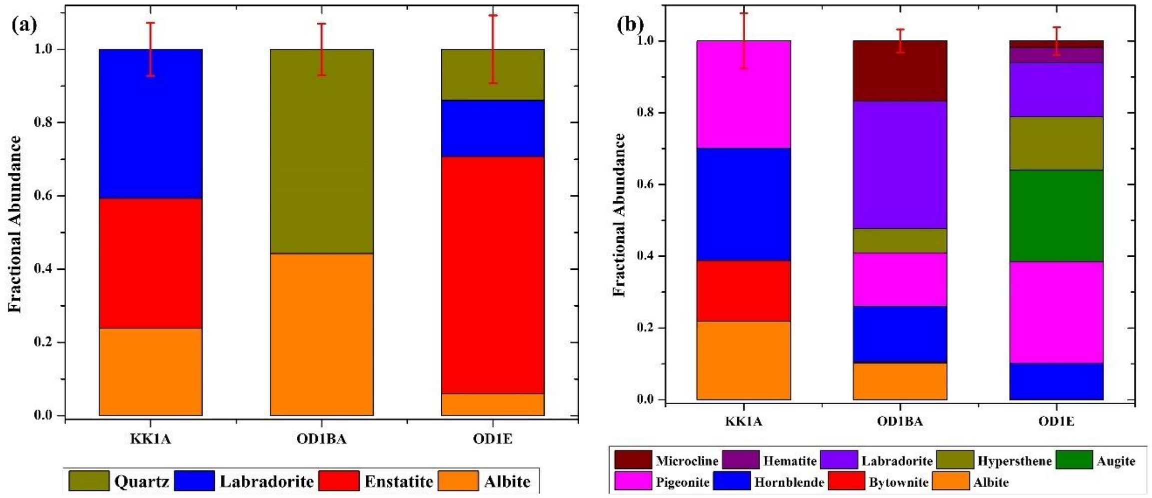

Figure S3 Mineral abundances and RMSE derived from (a) LMM in the TIR region and (b) PPNM in the VNIR region.

6 Text S2: **Decorrelation Stretch Images from THEMIS Datasets**

The DCS of THEMIS images were used to identify the high silica or quartz content. The identification of spectrally unique surfaces was obtained using the DCS images with bands 8-7-5, 9-6-4, and 6-4-2 in RGB colour composite. The DCS 8-7-5 RGB colour composite image is used to distinguish mafic and felsic minerals. The mafic minerals exhibit low emissivity at bands 6-9 (10.21-11.79 µm), and felsic minerals exhibit emissivity minima at band 5 (9.35 µm) (Lyon, 1965). Therefore, the regions with a high abundance of mafic minerals appear red, cyan and purple, whereas those with a high abundance of felsic minerals appear yellow (Figure S4). The DCS 9-6-4 and 6-4-2 RGB colour composite images were used to distinguish high silica or quartz content from other minerals. The quartz shows low emissivity at band 4 (8.56 µm). As a result, regions that appear yellow in the THEMIS DCS 9-6-4 image and magenta in the THEMIS DCS 6-4-2 image show a high abundance of quartz in the study area (Figures S5 and S6). The results from the DCS images suggest that the six selected study regions in the northern part of the Hellas basin are characterised by a high abundance of quartz and mafic minerals.

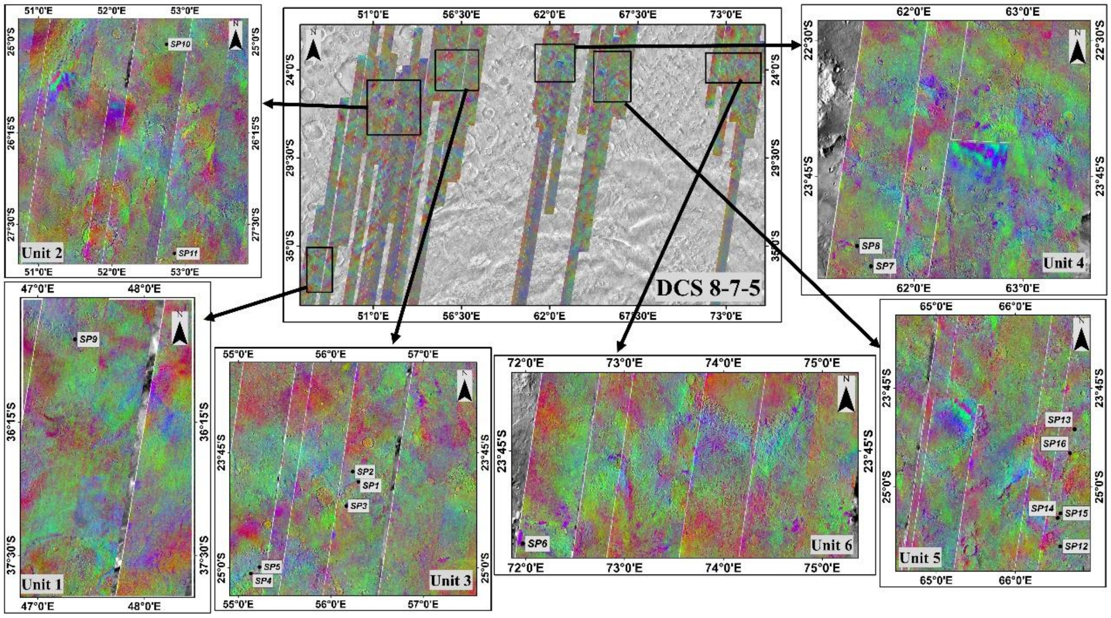

Figure S4 THEMIS DCS 8-7-5 RGB colour composite mosaic image (inset images from unit 1 to unit 6) overlaid on THEMIS global daytime mosaic covering a region of high mafic and felsic mineral deposits over the northern part of Hellas basin.

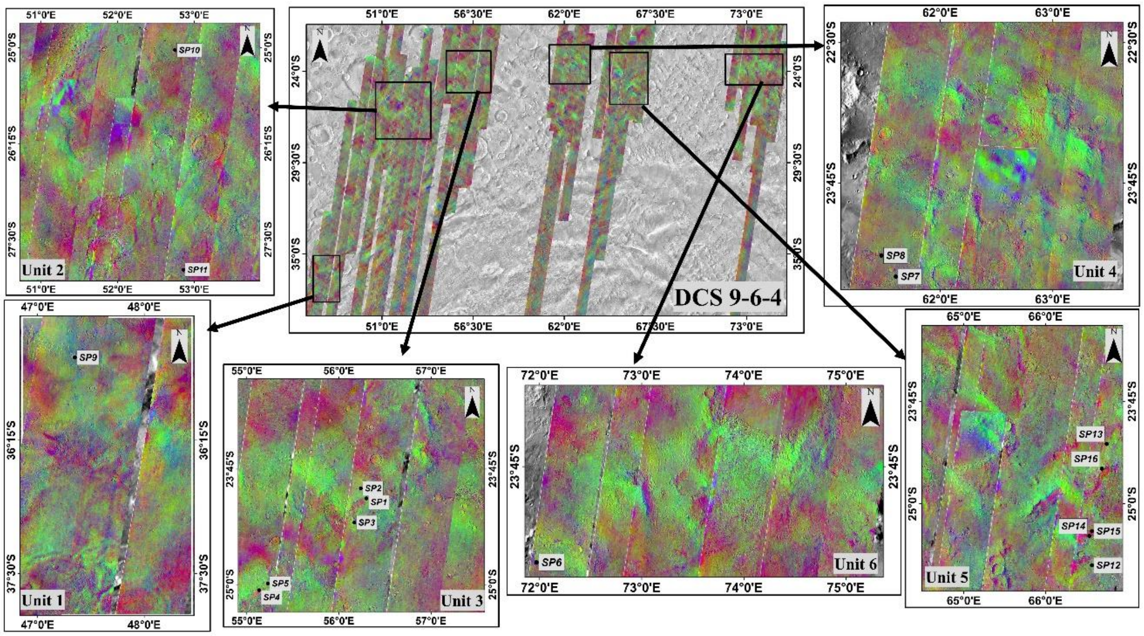

Figure S5 THEMIS DCS 9-6-4 RGB colour composite mosaic image (inset images from unit 1 to unit 6) overlaid on THEMIS global daytime mosaic covering a region of quartz deposits over the northern part of Hellas basin.

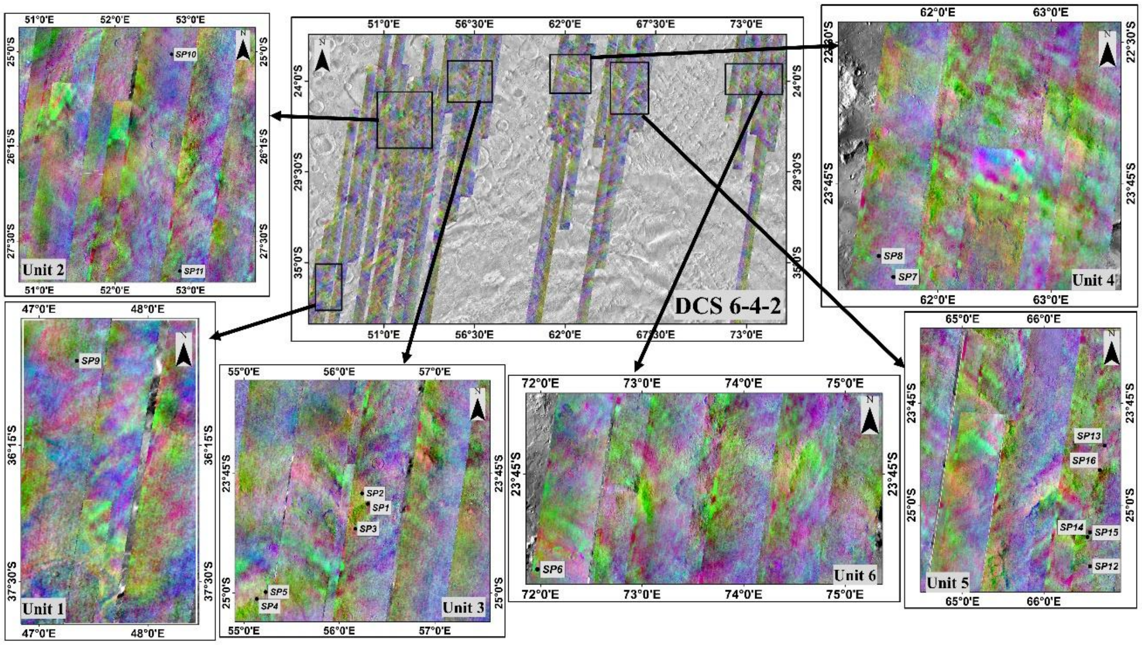

Figure S6 THEMIS DCS 6-4-2 RGB colour composite mosaic image (inset images from unit 1 to unit 6) overlaid on THEMIS global daytime mosaic covering the quartz deposits in the northern part of Hellas basin.

7 Text S3: Spatial Distribution of Mafic Minerals

The CRISM MAF browse products were used to obtain the spatial variation of mafic mineralogy over the six units in the northern part of the Hellas basin (Figure S7). The MAF browse image highlights the regions with mafic minerals. The regions with a high abundance of olivine appear in red in the image. The image shows the high abundance of LCP in green and cyan colours. Similarly, the high abundance of HCP appears blue and magenta in the image (Figure S7). The results from the MAF browse image indicate the presence of a high abundance of olivine (red) and LCP (green), along with a high abundance of HCP covering the northern part of the Hellas basin. Hence, the MAF browse product suggests the dominance of mafic minerals.

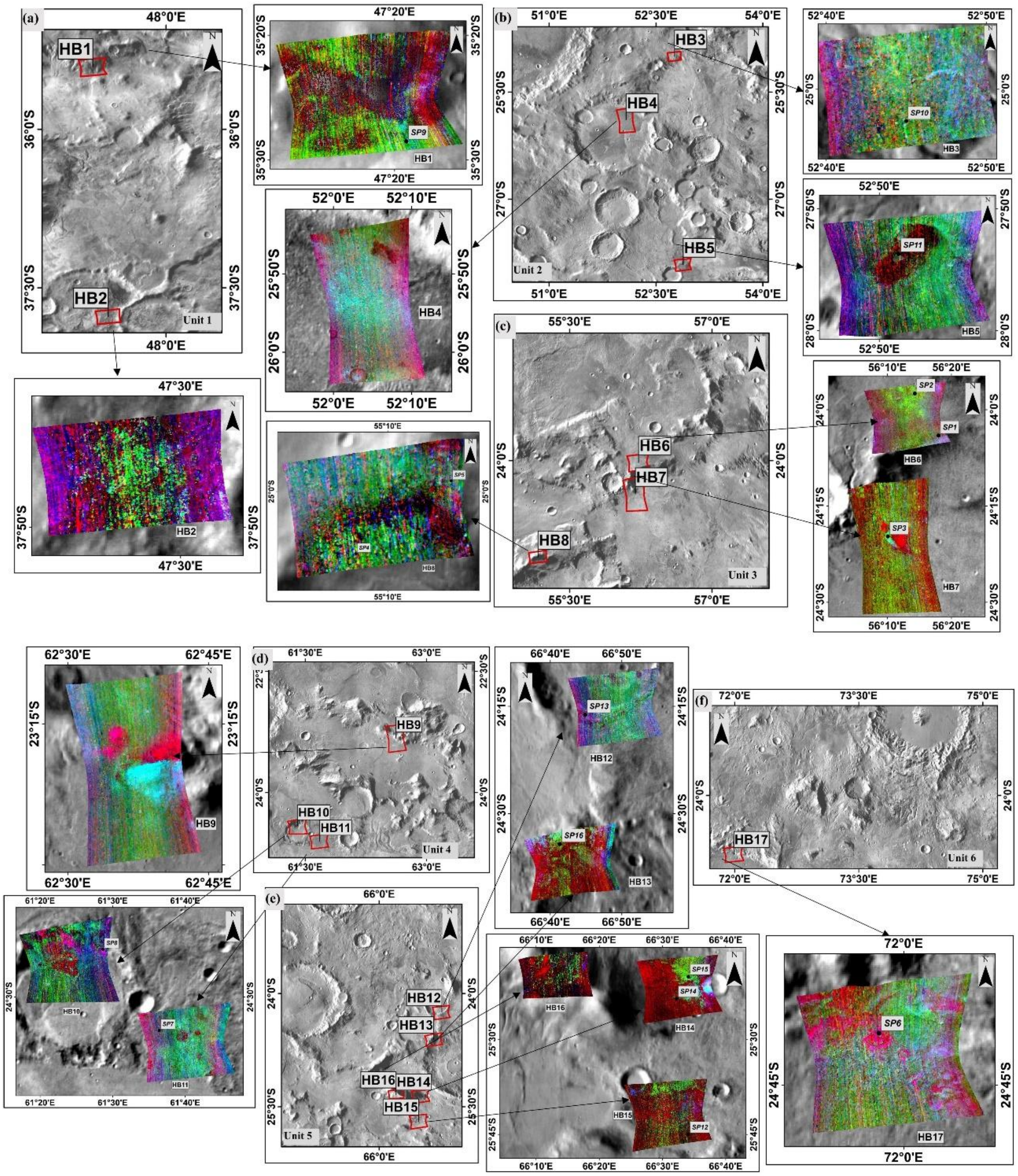

Figure S7 MAF browse product (R: OLINDEX3, G: LCPINDEX2, B: HCPINDEX2) overlaid on the THEMIS global daytime mosaic of northern regions of Hellas basin with the potential mafic minerals marked (SP1 to SP16) in the images.

In addition, the results from the THEMIS DCS RGB composite images (Figures S4, S5, and S6) indicate that the study regions are characterised by high quartz content. Therefore, spectra from potential regions showing the coexistence of high mafic and quartz content were extracted from both THEMIS and CRISM images. Locations of extracted spectra

(SP1 to SP16) from THEMIS and CRISM images. zoomed-in THEMIS DCS RGB composites are given in Figures S8 and S9.

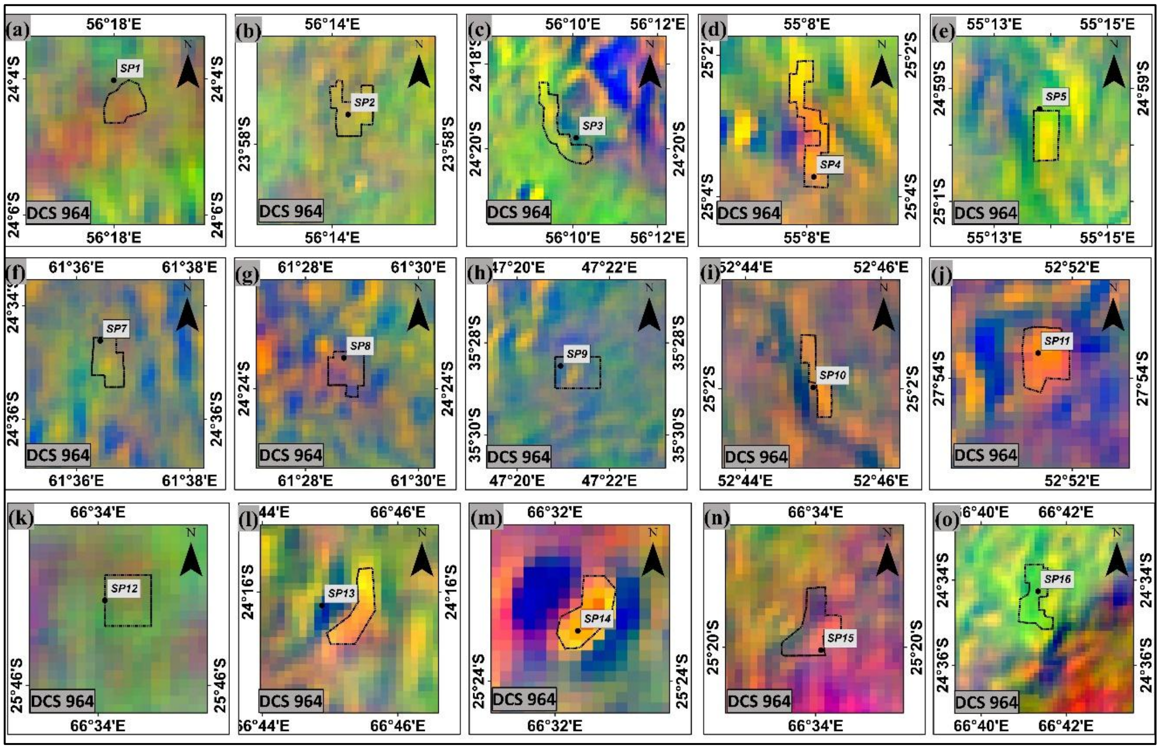

Figure S8 Locations of extracted spectra (SP1 to SP16) from THEMIS and CRISM images. Black boxes mark the Regions of Interest (ROIs) in the THEMIS images, while black dots indicate spectral points extracted from CRISM images. The background shows zoomed-in THEMIS DCS 9-6-4 RGB composites.

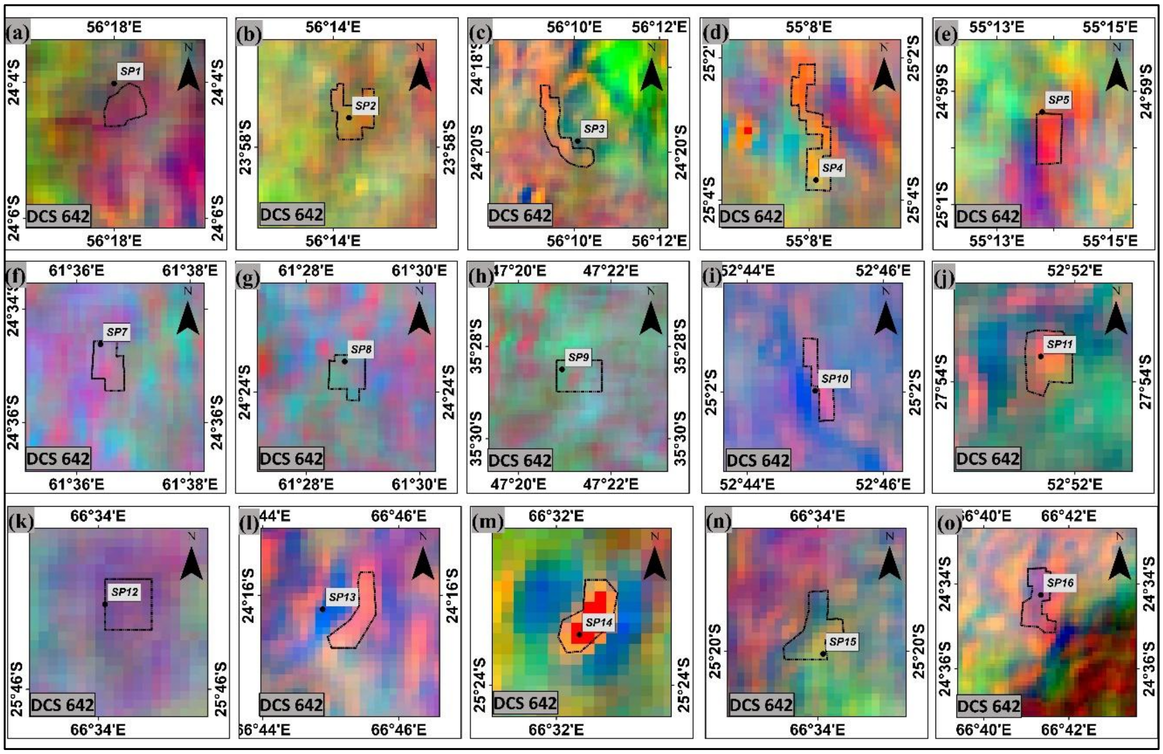

Figure S9 Locations of extracted spectra (SP1 to SP16) from THEMIS and CRISM images. Black boxes mark the Regions of Interest (ROIs) in the THEMIS images, while black dots indicate spectral points extracted from CRISM images. The background shows zoomed-in THEMIS DCS 6-4-2 RGB composites.

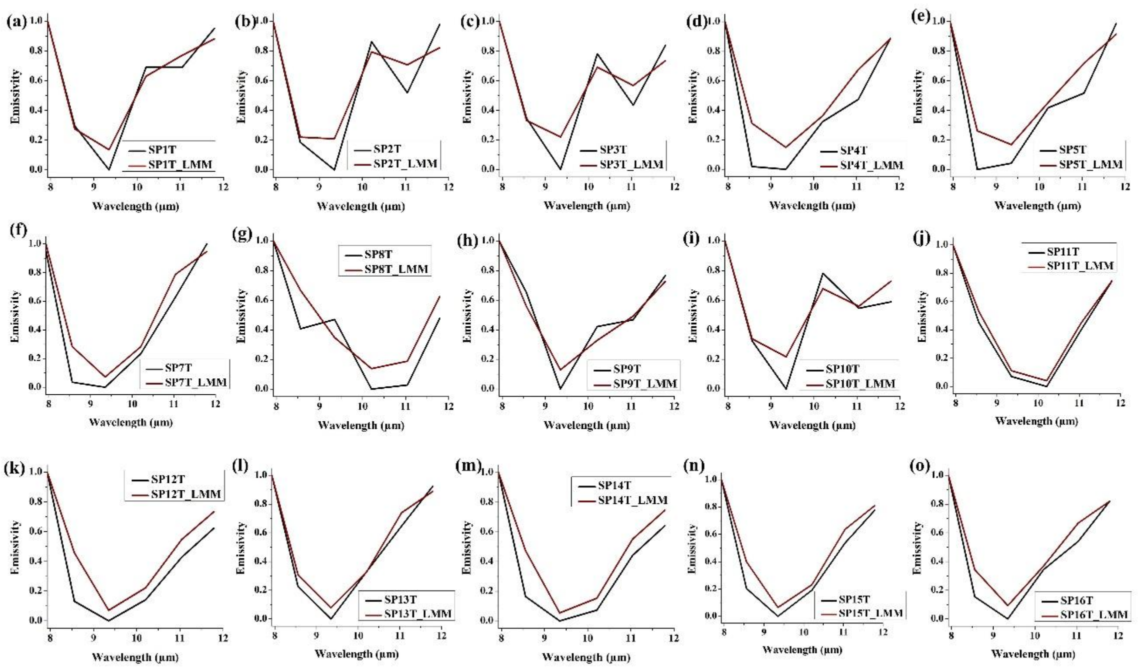

Figure S10 Spectral matching of emissivity spectra from THEMIS image and modelled spectra using LMM. The black colour represents emissivity spectra from the THEMIS image, and the red colour represents LMM-modelled spectra.

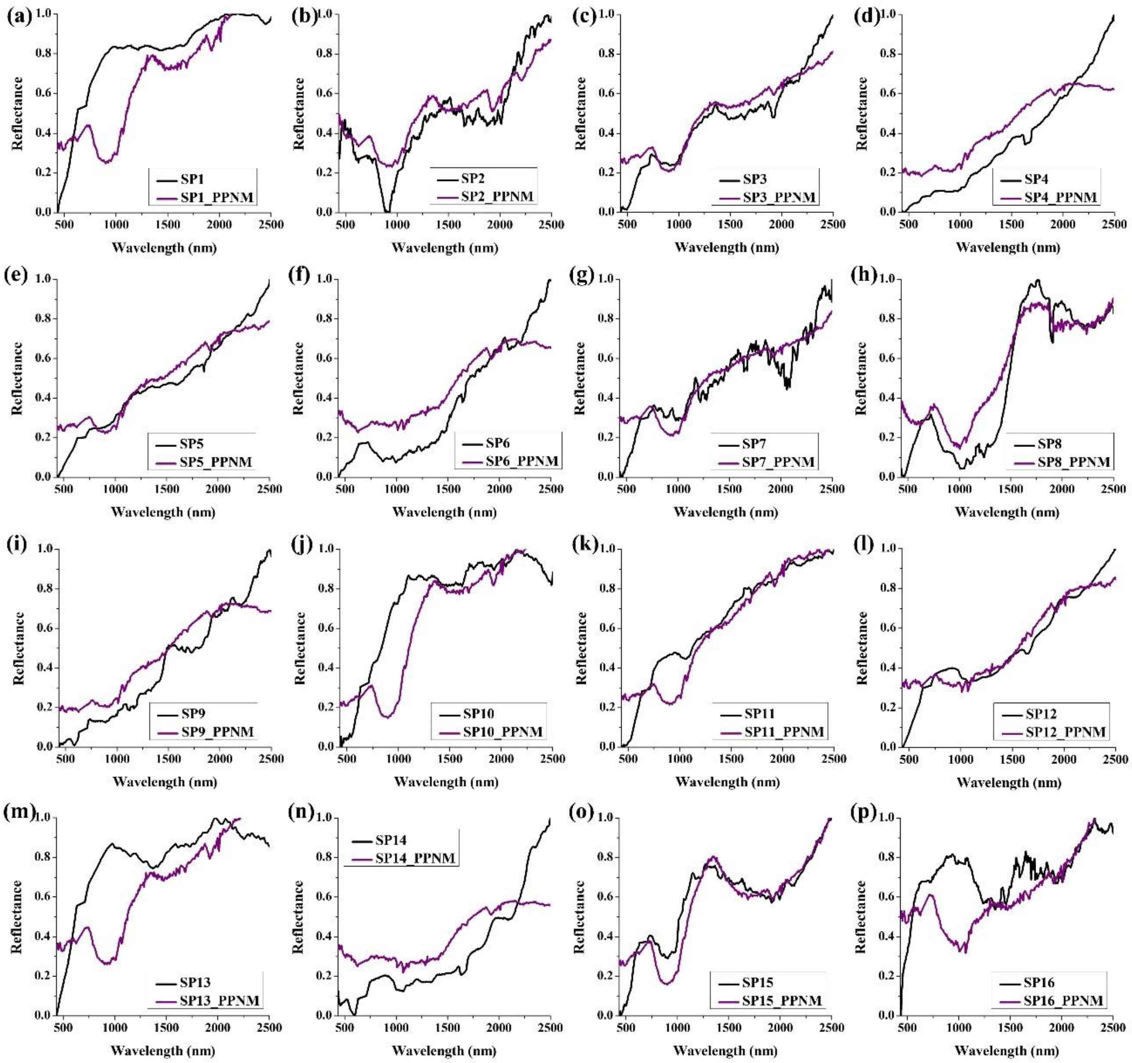

Figure S11 Spectral matching of reflectance spectra from CRISM image and modelled spectra using the PPNM model. The black colour represents reflectance spectra from the CRISM image, and the purple colour represents PPNM-modelled spectra.

Table S6a Statistics of the THEMIS image-derived spectrum SP1T, including maximum, minimum, and standard deviation values

Wavelength (µm)	Min	Max	Mean	Stdev
6.780	0.879	0.986	0.935	0.026
6.780	0.901	0.964	0.934	0.018
7.930	0.990	0.990	0.990	0.000
8.560	0.960	0.982	0.971	0.006
9.350	0.946	0.978	0.963	0.007
10.210	0.968	0.998	0.982	0.007
11.040	0.972	0.991	0.982	0.005
11.790	0.981	1.001	0.989	0.005
12.570	0.918	0.943	0.931	0.005
14.880	0.158	0.185	0.171	0.006

Table S6b Statistics of the THEMIS image-derived spectrum SP2T, including maximum, minimum, and standard deviation (Stdev) values

Wavelength (µm)	Min	Max	Mean	Stdev
6.780	0.879	0.952	0.924	0.016
6.780	0.884	0.951	0.916	0.016
7.930	0.990	0.990	0.990	0.000
8.560	0.964	0.993	0.978	0.005
9.350	0.964	0.983	0.975	0.004
10.210	0.977	0.998	0.988	0.004
11.040	0.971	0.995	0.983	0.005
11.790	0.977	1.007	0.990	0.006
12.570	0.916	0.949	0.935	0.007
14.880	0.134	0.165	0.150	0.006

Table S6c Statistics of the THEMIS image-derived spectrum SP3T, including maximum, minimum, and standard deviation (Stdev) values

Wavelength (µm)	Min	Max	Mean	Stdev
6.780	0.855	0.969	0.918	0.020
6.780	0.877	0.974	0.923	0.018
7.930	0.990	0.990	0.990	0.000

8.560	0.954	0.992	0.976	0.006
9.350	0.952	0.986	0.969	0.006
10.210	0.965	0.997	0.985	0.006
11.040	0.960	0.999	0.978	0.007
11.790	0.965	1.011	0.987	0.008
12.570	0.912	0.950	0.929	0.008
14.880	0.130	0.180	0.155	0.010

Table S6d Statistics of the THEMIS image-derived spectrum SP4T, including maximum, minimum, and standard deviation (Stdev) values

Wavelength (μm)	Min	Max	Mean	Stdev
6.780	0.959	1.036	0.997	0.017
6.780	0.953	1.027	0.991	0.014
7.930	0.992	0.992	0.992	0.000
8.560	0.934	0.983	0.963	0.008
9.350	0.941	0.988	0.963	0.007
10.210	0.953	1.000	0.972	0.009
11.040	0.959	1.004	0.977	0.008
11.790	0.968	1.011	0.989	0.010
12.570	0.919	0.964	0.941	0.012
14.880	0.133	0.160	0.145	0.006

Table S6e Statistics of the THEMIS image-derived spectrum SP5T, including maximum, minimum, and standard deviation (Stdev) values

Wavelength (μm)	Min	Max	Mean	Stdev
6.780	0.953	1.007	0.981	0.013
6.780	0.936	0.997	0.976	0.015
7.930	0.992	0.992	0.992	0.000
8.560	0.951	0.972	0.960	0.004
9.350	0.953	0.969	0.961	0.004
10.210	0.964	0.983	0.973	0.005
11.040	0.962	0.994	0.977	0.008
11.790	0.982	1.005	0.992	0.007
12.570	0.919	0.953	0.935	0.008
14.880	0.137	0.154	0.144	0.005

Table S6f Statistics of the THEMIS image-derived spectrum SP7T, including maximum, minimum, and standard deviation (Stdev) values

Wavelength (µm)	Min	Max	Mean	Stdev
6.780	0.982	1.015	0.996	0.007
6.780	0.980	1.014	0.998	0.009
7.930	0.983	0.983	0.983	0.000
8.560	0.973	0.988	0.978	0.003
9.350	0.968	0.989	0.978	0.004
10.210	0.970	0.988	0.979	0.004
11.040	0.975	0.988	0.982	0.003
11.790	0.978	0.992	0.983	0.003
12.570	0.918	0.931	0.926	0.003
14.880	0.147	0.160	0.154	0.003

Table S6g Statistics of the THEMIS image-derived spectrum SP8T, including maximum, minimum, and standard deviation (Stdev) values

Wavelength (µm)	Min	Max	Mean	Stdev
6.780	0.982	1.017	0.999	0.008
6.780	0.986	1.020	0.998	0.007
7.930	0.983	0.983	0.983	0.000
8.560	0.969	0.986	0.978	0.004
9.350	0.974	0.986	0.978	0.003
10.210	0.967	0.984	0.974	0.004
11.040	0.964	0.981	0.975	0.004
11.790	0.971	0.987	0.979	0.004
12.570	0.913	0.929	0.921	0.004
14.880	0.136	0.157	0.147	0.004

Table S6h Statistics of the THEMIS image-derived spectrum SP9T, including maximum, minimum, and standard deviation (Stdev) values

Wavelength (μm)	Min	Max	Mean	Stdev
6.780	0.958	1.008	0.982	0.013
6.780	0.958	1.008	0.983	0.012
7.930	0.992	0.992	0.992	0.000
8.560	0.966	0.985	0.978	0.005
9.350	0.939	0.965	0.952	0.006
10.210	0.958	0.980	0.969	0.005
11.040	0.960	0.985	0.971	0.005
11.790	0.969	0.993	0.982	0.005
12.570	0.897	0.923	0.910	0.005
14.880	0.170	0.183	0.176	0.003

Table S6i Statistics of the THEMIS image-derived spectrum SP10T, including maximum, minimum, and standard deviation (Stdev) values

Wavelength (µm)	Min	Max	Mean	Stdev
6.780	0.975	1.010	0.989	0.008
6.780	0.969	1.009	0.984	0.010
7.930	0.993	0.993	0.993	0.000
8.560	0.971	0.995	0.984	0.005
9.350	0.970	0.992	0.980	0.005
10.210	0.977	1.004	0.990	0.007
11.040	0.975	1.001	0.987	0.007
11.790	0.976	1.008	0.988	0.009
12.570	0.923	0.959	0.940	0.009
14.880	0.100	0.117	0.107	0.004

Table S6j Statistics of the THEMIS image-derived spectrum SP11T, including maximum, minimum, and standard deviation (Stdev) values

Wavelength (µm)	Min	Max	Mean	Stdev
6.780	0.900	0.973	0.935	0.018
6.780	0.891	0.979	0.933	0.022
7.930	0.995	0.995	0.995	0.000
8.560	0.955	0.985	0.972	0.008
9.350	0.935	0.973	0.956	0.009
10.210	0.933	0.967	0.953	0.010
11.040	0.946	0.992	0.970	0.012
11.790	0.962	1.006	0.984	0.011
12.570	0.906	0.952	0.930	0.011
14.880	0.182	0.279	0.237	0.020

Table S6k Statistics of the THEMIS image-derived spectrum SP12T, including maximum, minimum, and standard deviation (Stdev) values

Wavelength (μm)	Min	Max	Mean	Stdev
6.780	0.914	0.998	0.959	0.022
6.780	0.914	0.997	0.957	0.018
7.930	0.999	0.999	0.999	0.000
8.560	0.949	0.971	0.960	0.006
9.350	0.941	0.966	0.954	0.006
10.210	0.950	0.975	0.961	0.007
11.040	0.964	0.983	0.973	0.005
11.790	0.974	0.993	0.982	0.005
12.570	0.914	0.947	0.929	0.007
14.880	0.194	0.222	0.208	0.007

Table S6l Statistics of the THEMIS image-derived spectrum SP13T, including maximum, minimum, and standard deviation (Stdev) values

Wavelength (μm)	Min	Max	Mean	Stdev
6.780	0.897	0.973	0.936	0.018
6.780	0.911	0.999	0.947	0.018
7.930	0.999	0.999	0.999	0.000
8.560	0.952	0.983	0.967	0.008
9.350	0.942	0.976	0.958	0.008
10.210	0.942	0.998	0.972	0.012
11.040	0.955	1.006	0.984	0.012
11.790	0.962	1.020	0.996	0.013
12.570	0.913	0.969	0.943	0.013
14.880	0.142	0.198	0.162	0.015

Table S6m Statistics of the THEMIS image-derived spectrum SP14T, including maximum, minimum, and standard deviation (Stdev) values

Wavelength (μm)	Min	Max	Mean	Stdev
6.780	0.782	0.992	0.918	0.046
6.780	0.849	1.047	0.928	0.039
7.930	0.999	0.999	0.999	0.000
8.560	0.949	0.990	0.964	0.009
9.350	0.932	0.981	0.957	0.011
10.210	0.911	0.983	0.960	0.019
11.040	0.912	1.009	0.976	0.026
11.790	0.910	1.019	0.984	0.032
12.570	0.853	0.966	0.930	0.033
14.880	0.185	0.289	0.229	0.030

Table S6n Statistics of the THEMIS image-derived spectrum SP15T, including maximum, minimum, and standard deviation (Stdev) values

Wavelength (µm)	Min	Max	Mean	Stdev
6.780	0.865	0.986	0.933	0.026
6.780	0.878	0.974	0.921	0.020
7.930	0.999	0.999	0.999	0.000
8.560	0.948	0.983	0.964	0.007
9.350	0.940	0.976	0.955	0.008
10.210	0.950	0.980	0.963	0.007
11.040	0.965	0.995	0.978	0.007
11.790	0.976	1.006	0.989	0.007
12.570	0.919	0.955	0.935	0.008
14.880	0.188	0.221	0.206	0.007

Table S6o Statistics of the THEMIS image-derived spectrum SP16T, including maximum, minimum, and standard deviation (Stdev) values

Wavelength (µm)	Min	Max	Mean	Stdev
6.780	0.880	0.986	0.920	0.019
6.780	0.876	0.959	0.918	0.018
7.930	0.999	0.999	0.999	0.000
8.560	0.953	0.979	0.967	0.005
9.350	0.943	0.975	0.961	0.006
10.210	0.953	0.988	0.974	0.007
11.040	0.961	0.998	0.981	0.008
11.790	0.964	1.015	0.992	0.009
12.570	0.908	0.962	0.937	0.010
14.880	0.155	0.183	0.172	0.006